JBC RESEARCH ARTICLE

The mammalian rhomboid protein RHBDL4 protects against endoplasmic reticulum stress by regulating the morphology and distribution of ER sheets

Received for publication, September 8, 2021, and in revised form, March 24, 2022 Published, Papers in Press, April 15, 2022,
https://doi.org/10.1016/j.jbc.2022.101935

Viorica L. Lastun*, Clémence Levet, and Matthew Freeman*
From the Dunn School of Pathology, Oxford, United Kingdom

Edited by Ursula Jakob

In metazoans, the architecture of the endoplasmic reticulum (ER) differs between cell types and undergoes major changes throughout the cell cycle and according to physiological needs. Although much is known about how the different ER morphologies are generated and maintained, especially ER tubules, how context-dependent changes in ER shape and distribution are regulated and the factors involved are less well characterized, as are the factors that contribute to the positioning of the ER within the cell. By overexpression and KO experiments, we show that the levels of RHBDL4, an ER-resident rhomboid protease, modulate the shape and distribution of the ER, especially during conditions that require rapid changes in the ER sheet distribution, such as ER stress. We demonstrate that RHBDL4 interacts with cytoskeleton-linking membrane protein 63 (CLIMP-63), a protein involved in ER sheet stabilization, as well as with the cytoskeleton. Furthermore, we found that mice lacking RHBDL4 are sensitive to ER stress and develop liver steatosis, a phenotype associated with unresolved ER stress. Taken together, these data suggest a new physiological role for RHBDL4 and also imply that this function does not require its enzymatic activity.

The endoplasmic reticulum (ER) is the largest membrane-bound organelle of eukaryotic cells, comprising the nuclear envelope and peripheral ER. In metazoans, the peripheral ER spreads throughout the cytoplasm as a network of interconnected flat sheets and tubules; the flat sheets are present mostly around the nucleus, whereas the tubules interconnect at the level of three-way junctions generating a reticular network toward the cell periphery (1, 2). The two distinct ER morphologies accommodate different functions. The sheets are studded with ribosomes and form the rough ER, the site of import, folding, and quality control of secreted and transmembrane proteins, and are abundant in professional secretory cells (3, 4). The tubules mostly lack ribosomes and form the smooth ER, associated with lipid synthesis and Ca^{2+} signaling/homeostasis, abundant in steroid-secreting cells (3–6). The ER tubules also engage in contacts with other membrane-bound as well as membraneless organelles, and a role is emerging for the ER in regulating the biogenesis and/or the dynamics of organelles with which it shares contact sites (7, 8).

Several proteins that shape the ER have been discovered. Reticulons (RTNs) and receptor expression–enhancing proteins (REEPs) generate the high membrane curvature characteristic of ER tubules, whereas atlastins (ATLs) mediate the homotypic fusion of ER membranes (9–14). ER sheets have a more complex structure, and less is known about how they are generated and maintained. RTNs generate the curvature at sheet edges, and several components have been shown to stabilize the flat sheets, including the coiled-coil proteins cytoskeleton-linking membrane protein 63 (CLIMP-63), p180, and kinectin, the attached polysomes engaged in protein translation, as well as the actin cytoskeleton through myosin 1c (4, 15, 16). None of these factors, however, are essential for the existence of ER sheets, suggesting additional structural and regulatory complexity. Beyond its morphology, the factors that contribute to the positioning of the ER within the cell are also not well established; again, more is known about tubules than sheets. ER tubules are often situated along microtubules, and their growth and movement in the cell rely largely on this interaction (17–19). ER sheet proteins CLIMP-63 and p180 can bind to microtubules, and cytoskeleton depolymerization was shown to change ER sheet distribution (15, 20, 21), although the mechanisms involved in positioning and the dynamics of the ER sheets remain poorly understood. The ER network varies in volume, shape, and distribution between cell types, and it undergoes reorganization through the cell cycle, differentiation, and according to physiological needs (3, 22, 23), implying the need for regulation. The abundance of ER-shaping proteins is a determining factor of the sheet to tubule ratio: high levels of RTNs and REEPs favor the abundance of tubules over the ER sheets, whereas CLIMP-63 has the opposite effect (4, 24). Overall, though, rather little is known about the regulation of the rapid and complex changes in ER morphology and distribution in different cellular contexts.

One challenge to ER function, and implicitly to its morphology and distribution, is ER stress. The homeostasis of

* For correspondence: Matthew Freeman, matthew.freeman@path.ox.ac.uk; Viorica L. Lastun, viorica.liebe@oncology.ox.ac.uk.
Present address for Viorica L. Lastun: MRC Weatherall Institute of Molecular Medicine, John Radcliffe Hospital, Oxford, United Kingdom.

protein folding in the ER is essential for healthy cells and organisms and is maintained by a balance between protein biosynthesis and folding on one hand and export and degradation on the other. Conditions that perturb this homeostasis, generically referred to as ER stress, lead to the accumulation of unfolded proteins in the ER lumen and the activation of the unfolded protein response (UPR). The UPR is an integrated signaling network from the ER to cytoplasm and nucleus, which counteracts the effects of ER stress by upregulating ER chaperones, folding enzymes, and components of the ER-associated protein degradation (ERAD) machinery, while also reducing protein translation (25, 26). ER stress also causes significant changes in the size, morphology, and distribution of the ER in mammalian and yeast cells (27, 28).

RHBDL4 (aka RHBDD1) is a member of the rhomboid intramembrane serine protease family; it is localized in the ER and is upregulated by ER stress (29, 30). Although its overall core function remains mysterious, several roles have been assigned to RHBDL4. Its increased expression has been correlated with cancer progression (31, 32). RHBDL4 has also been shown to activate epidermal growth factor receptor (EGFR) signaling by promoting the secretion in extracellular microvesicles of transforming growth factor alpha (TGFα) (33, 34). And, in a more classic protease function, RHBDL4 is reported to cleave amyloid precursor protein (APP) (35). The most well characterized RHBDL4 function, and the one most apparently relevant to its ER localization, is a function in cleaving and promoting the degradation of various unstable proteins or orphan subunits of protein complexes (29, 36), implying that RHBDL4 participates in some forms of ERAD.

Here, we describe an unexpected role of RHBDL4 in regulating the shape and distribution of the ER. By gain- and loss-of-function experiments, we found that the levels of RHBDL4 modulate the shape and distribution of the ER, particularly under ER stress and when the cytoskeleton is disrupted, conditions that require rapid and dynamic changes in ER sheet distribution. We report that RHBDL4 interacts with CLIMP-63, and it potentially associates with the cytoskeleton. Unexpectedly, this role of RHBDL4 appears to be independent of its enzymatic activity, implying an additional, nonproteolytic, function of this intramembrane protease. Finally, we also show that RHBDL4 is essential for resolving acute ER stress in mice.

Results

The levels of RHBDL4 affect the ER organization

Overexpression of RHBDL4 disrupts ER morphology

RHBDL4 is an ER-resident protein (29). While doing transient transfections and immunofluorescence, we noticed that overexpressed RHBDL4 staining looked unusual in many cells. To characterize this within the context of ER organization, we used CLIMP-63 as a marker for ER sheets and reticulon 4 (RTN4) for the whole ER—RTNs reside in ER tubules and the edges of the ER sheets (4). When expressed at low levels, RHBDL4 showed a perinuclear localization, characteristic of ER sheets, similar to that of CLIMP-63 (Fig. 1*A*, *second column*, the cell indicated by *arrowhead*). At higher expression levels, RHBDL4 distributed widely into the ER and induced the appearance of punctate structures (Fig. 1*A*, *second and third columns*, the cells indicated by *arrow*). High expression levels of RHBDL4 led to a massive disruption in the appearance of the ER, especially at the level of ER sheets, as shown by CLIMP-63 distribution: CLIMP-63 was redistributed into tubules toward the cell periphery (Fig. 1*A*, *second column*, the cell indicated by *arrow*) or confined into compact structures around the nucleus (Fig. 1*A*, *third column*). The perinuclear staining of RTN4 was lost, and some of the protein was recruited to the RHBDL4-containing puncta (Fig. 1*A*, *second and third columns*, the cells indicated by *arrow*). Figure 1*A* (*first column*) shows the distribution of CLIMP-63 and RTN4 in a nontransfected cell.

Overexpression of an RHBDL4 mutant that had the catalytic serine replaced by an alanine—RHBDL4 S144A (37)—showed similar results: increased levels of RHBDL4 S144A led to a similar disruption of the ER architecture (Fig. 1*B*, the cells in the *second and third columns*, compared with the cell in the *first column*), suggesting that the proteolytic activity of RHBDL4 is not required in this context. This disruption of ER morphology was specific to RHBDL4: the overexpression of another rhomboid protease, RHBDL3, which is structurally very similar to RHBDL4, did not induce changes in the ER morphology, even when expressed at very high levels (Fig. S1). To make this a more rigorous control for ER-localized RHBDL4, RHBDL3, which normally moves through the ER to its primary plasma membrane location (30), was artificially retained in the ER by the addition of a KDEL retention sequence at its C terminus (38).

RHBDL4 KO affects the ER sheet distribution

Given the effect of RHBDL4 overexpression on the ER, we hypothesized that RHBDL4 plays a role in the ER shape and/or distribution under physiological conditions. To test this, we used two different RHBDL4 KO cell lines—mouse embryonic fibroblasts (MEFs) and human HeLa cells—and compared their ER distribution to that of their WT counterparts.

In WT and RHBDL4 KO MEFs, CLIMP-63 had a similar distribution (Fig. 2*A*). To confirm this, we quantified the signal distribution using CellProfiler-3.0.0 (39). The area between the nucleus and plasma membrane was divided into 10 bins (Fig. 2*B*), and the mean fractional intensity at a given radius was calculated as fraction of total intensity, normalized by the fraction of pixels at that radius. Indeed, there was no difference between WT and RHBDL4 KO MEFs (Fig. 2*C*). As RHBDL4 was shown to be upregulated in response to ER stress (29), we asked whether RHBDL4 is important for the ER shape changes that occur during ER stress. We challenged the cells with tunicamycin, an inhibitor of N-linked glycosylation that leads to accumulation of misfolded proteins in the ER and therefore induces ER stress (40, 41). In WT MEFs, after 24 h of tunicamycin treatment, CLIMP-63 redistributed dramatically throughout the cytoplasm as compared with the control (Fig. 2*D*, *upper row*), implying a major reorganization of ER sheets. In contrast, CLIMP-63 redistribution was abnormal in

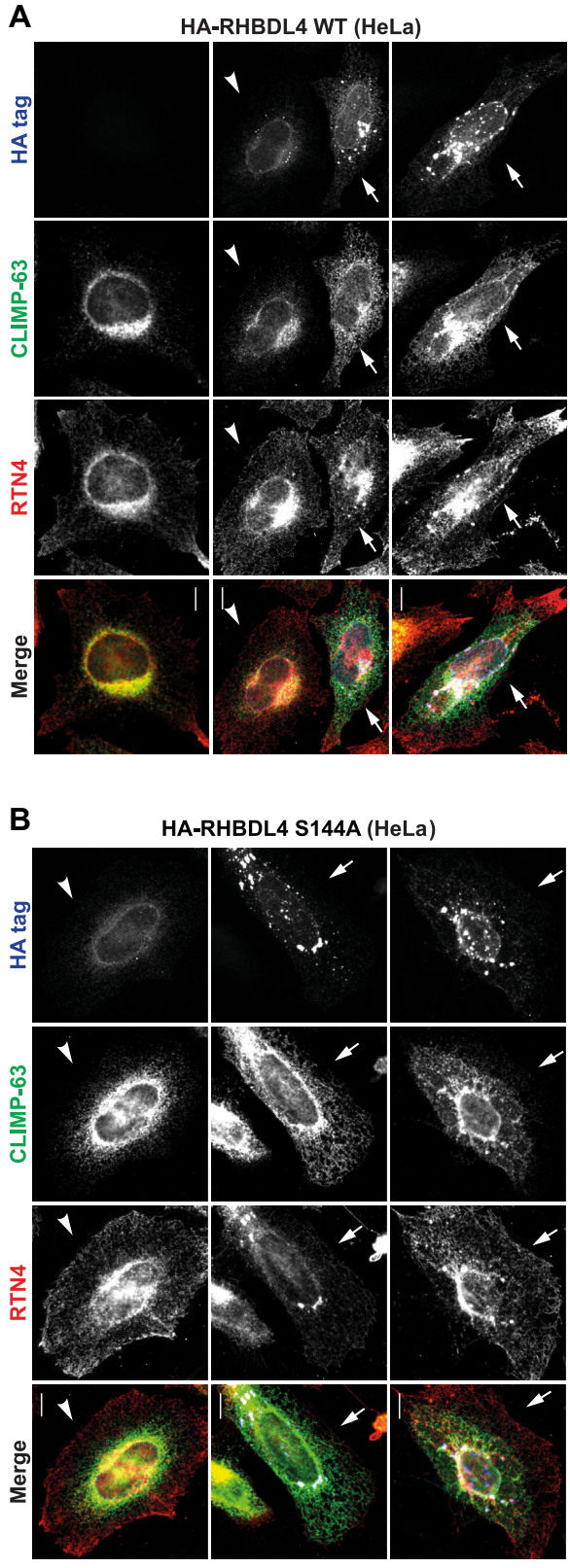

Figure 1. RHBDL4 overexpression disrupts ER organization. *A*, immunofluorescence images of RHBDL4 overexpression in HeLa cells. Cells were transfected with HA-tagged RHBDL4 and, after 24 h, stained for HA tag (*blue*), CLIMP-63 (*green*), and RTN4 (*red*). *B*, overexpression of HA-tagged RHBDL4 S144A in HeLa cells, analyzed as in *A*. The scale bar represents 10 μm. The *arrowhead* and *arrows* indicate cells with low and high RHBDL4 expression levels, respectively. The images are representative of at least three independent experiments. CLIMP-63, cytoskeleton-linking membrane protein 63; ER, endoplasmic reticulum; HA, hemagglutinin; RTN4, reticulon 4.

RHDBL4 KO MEFs, with 28.76% of cells showing a strong phenotype, with a "collapse" of CLIMP-63 signal around the nucleus (Fig. 2*D*, *lower row*, and quantified in Fig. 2*E*, *upper panel*). This phenotype was significantly rescued by transient transfection of RHBDL4 WT (Fig. 2*E*—quantification is shown in the *upper panel* and a representative image in the *lower panel*), indicating that the effect was specific to loss of RHBDL4. We could not detect rescue when using the RHBDL4 S144A mutant (data not shown), but this result is hard to interpret because expression of this mutant, even at low levels, induces acute ER stress on its own (29) (Fig. S2, lanes 3 and 4 compared with lanes 7 and 8). It is therefore likely that its expression combined with tunicamycin treatment induced very high levels of ER stress in RHBDL4 KO cells, preventing a rescue of ER morphology.

In WT HeLa cells, the distribution of CLIMP-63 and RTN4 followed their expected localization: CLIMP-63, marking ER sheets, was more concentrated within the innermost bins, whereas RTN4, marking ER tubules, was distributed more widely toward the plasma membrane (Fig. 3, *A* and *B*). The ER was more compacted around the nucleus in the RHBDL4 KO cells when compared with the WT, especially when looking at CLIMP-63 (Fig. 3*A*, *lower row*, and quantified in Fig. 3, *C* and *D*). Transient transfection of the RHBDL4 KO cells with either WT or the catalytically inactive RHBDL4 rescued the phenotype (Fig. 3*E*—quantification is shown in the *left panel*, and representative images are shown in the *right panel*), supporting the conclusion that the role of RHBDL4 in ER sheet distribution is not dependent on its proteolytic activity.

As in MEFs, tunicamycin treatment of WT HeLa cells led to a redistribution of CLIMP-63 throughout the cytoplasm. Interestingly, RTN4 did not follow the same pattern, suggesting that the proliferated (and perhaps dilated) ER sheets did not contain as much RTN4 as when packed in the perinuclear area (Fig. 3*F*, *upper row*, and quantified in Fig. S3). When looking at CLIMP-63, in RHDBL4 KO, a subset of cells showed a pronounced phenotype of more concentrated perinuclear staining and a nonhomogeneous distribution toward the cell periphery (Fig. 3, *F* and *G*).

Altogether, our results in MEFs and HeLa cells show that RHBDL4 is important for ER sheet distribution and that the effect was more pronounced during ER stress. Note that, in addition to the striking effect on ER sheets, this analysis cannot rule out a subtle effect of RHBDL4 on ER tubules, below the resolution of confocal imaging.

The levels of ER-shaping proteins and the ER stress response are similar in WT and RHBDL4 KO cells

The role of RHBDL4 in ER shape/distribution could be direct or indirect, *via* other ER-shaping proteins. Also, the phenotypes we described in RHBDL4 KO cells could be due to a defective folding/secretory function of the ER or failure to activate the UPR and cope with the ER stress. Analysis of

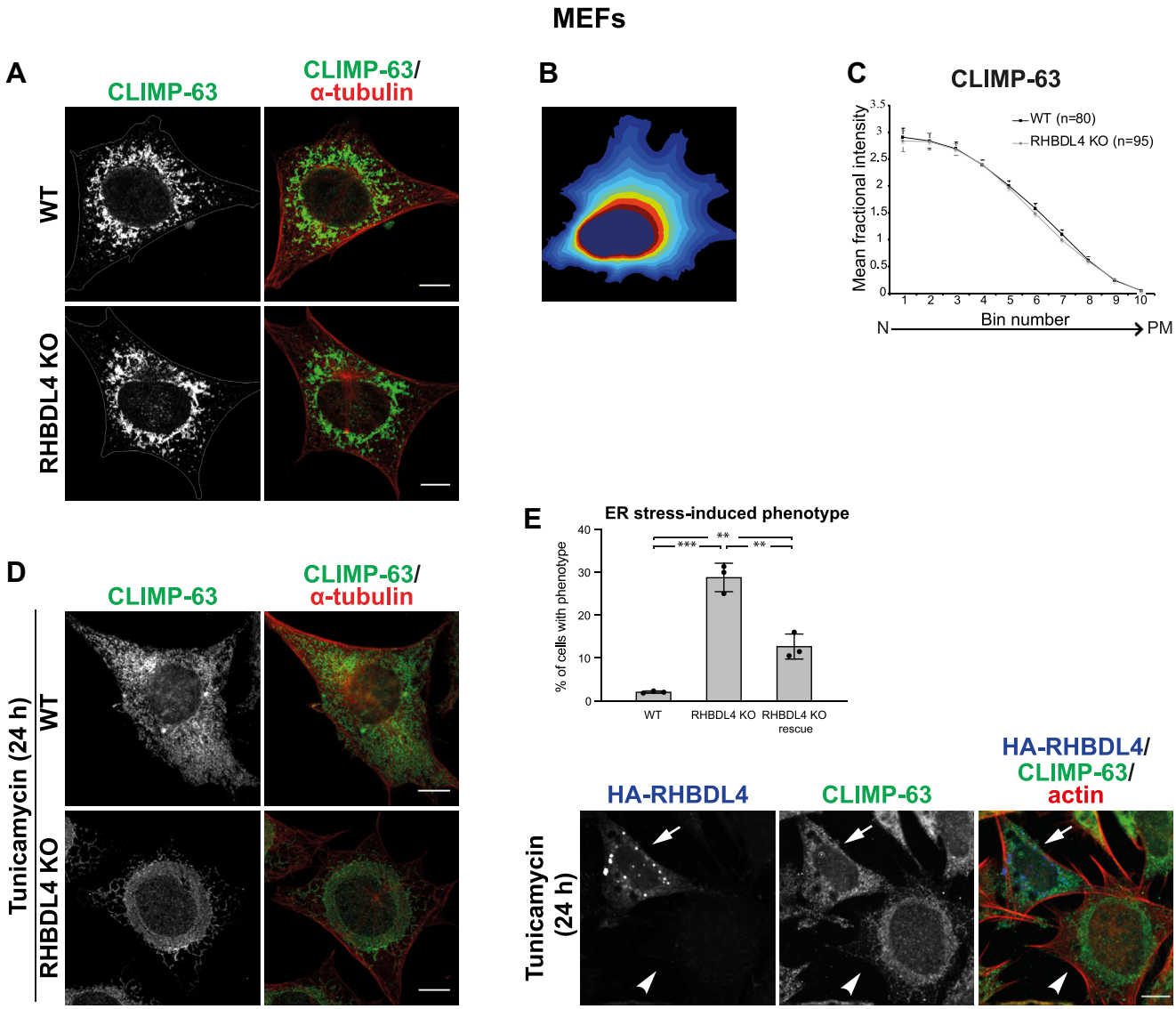

Figure 2. RHBDL4 affects ER distribution under ER stress conditions in MEFs. *A*, immunofluorescence of CLIMP-63 (*green*) and α-tubulin (*red*) in WT and RHBDL4 KO MEFs. *B*, a representation of the way the area between the nucleus and plasma membrane was divided into 10 bins to quantify the signal distribution. *C*, quantification of CLIMP-63 distribution. Error bars represent the 95% confidence interval (CI). *D*, as in *A*, but 24 h after tunicamycin treatment. The images and quantification are representative of three independent experiments. *E*, quantification of cells presenting a tunicamycin-induced phenotype, *upper panel*, and a representative immunofluorescence image from a rescue experiment, *lower panel*. For rescue experiments, RHBDL4 KO cells were transiently transfected with HA-tagged RHBDL4 WT. Error bars represent standard deviation (n = 3 experiments, with at least 50 cells/experiment analyzed for WT and RHBDL4 KO and at least 25 cells/experiment analyzed for rescue RHBDL4-HA). For WT *versus* RHBDL4 KO, $p = 0.0002$ *t* test, two-sided (three *asterisks* on the graph) and $p = 0.049$ Mann–Whitney–Wilcoxon test, two-sided. For rescue RHBDL4-HA *versus* RHBDL4 KO, $p = 0.0033$ *t* test (two *asterisks* on the graph) and $p = 0.049$ Mann–Whitney–Wilcoxon test, two-sided. For rescue RHBDL4-HA *versus* WT, $p = 0.0033$ *t* test (two *asterisks* on the graph) and $p = 0.049$ Mann–Whitney–Wilcoxon test, two-sided. In all images, the scale bar represents 10 μm. CLIMP-63, cytoskeleton-linking membrane protein 63; ER, endoplasmic reticulum; HA, hemagglutinin; MEF, mouse embryonic fibroblast.

MEFs and HeLa cells by Western blot showed no obvious differences in the levels of RTN4, ATL1, or CLIMP-63 between WT and RHBDL4 KO, either in control or under induced ER stress conditions (Figs. 4*A* and S4*A*, respectively). This implies that RHBDL4 does not affect the levels of these ER-shaping proteins.

We next asked whether RHBDL4 affects the ER stress response. Under ER stress, to cope with the folding load, cells increase their protein folding capacity by activating the UPR (42). Two of the chaperones that are upregulated most in response to ER stress are immunoglobulin binding protein (BiP) and glucose-regulated protein 94 (GRP94) (43). As shown in Figures 4*B* and S4*B*, BiP and GRP94 upregulation by tunicamycin treatment was similar in WT and RHBDL4 KO cells (both BiP and GRP94 were detected using an anti-KDEL antibody). Failure to restore protein homeostasis in the ER results in activation of apoptosis. We assayed a central mediator of apoptosis, the proapoptotic transcription factor C/EBP homologous protein (CHOP) (44), and found similar levels in WT and RHBDL4 KO MEFs (Fig. 4*B*). We conclude that the ER stress response is not significantly affected in these RHBDL4 KO cells.

To assess the general secretory function of the ER in RHBDL4 KO cells, we examined the cellular location of

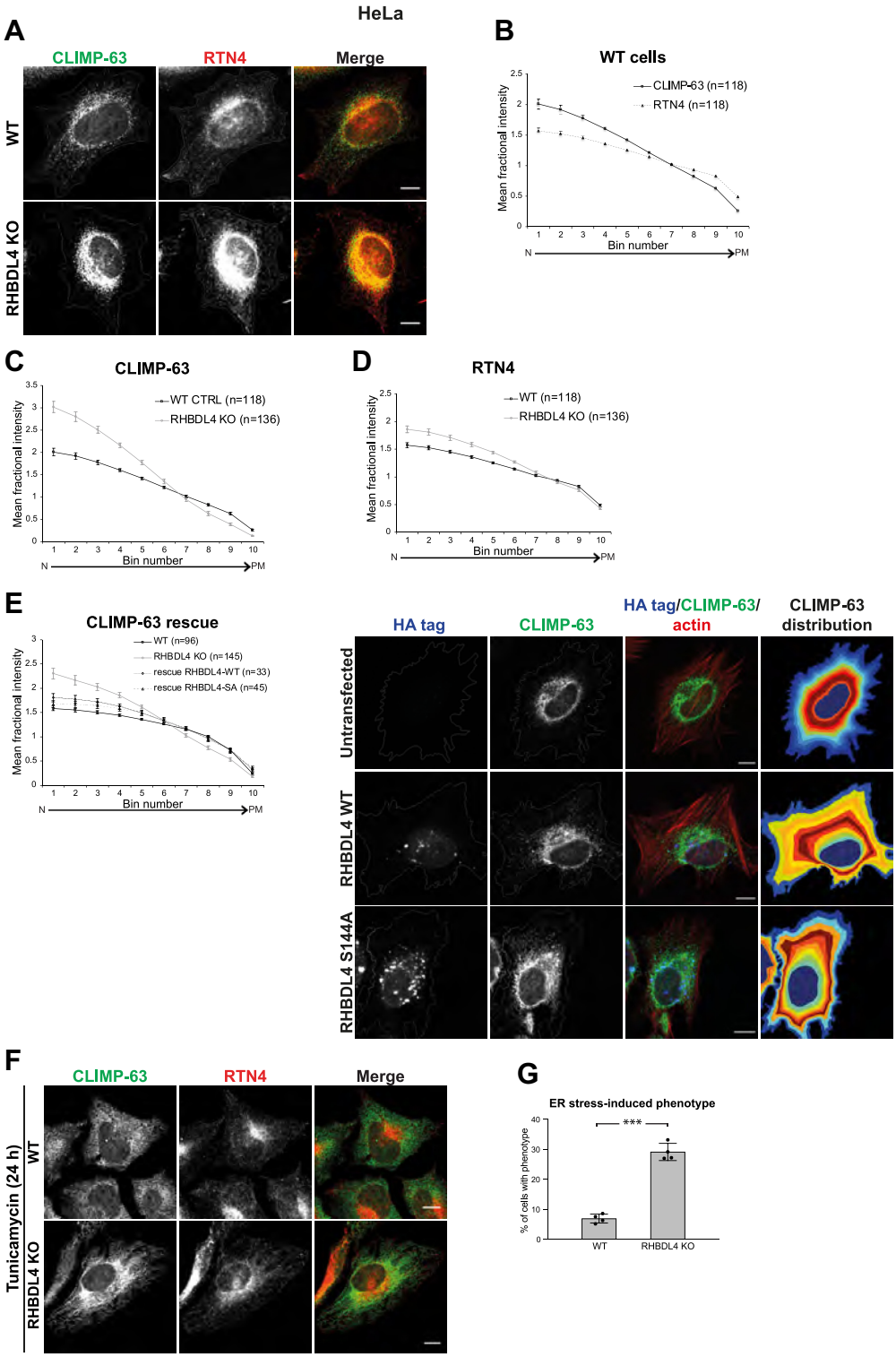

Figure 3. RHBDL4 affects ER distribution in HeLa cells. *A*, immunofluorescence of CLIMP-63 (*green*) and RTN4 (*red*) in WT and RHBDL4 KO HeLa cells. *B*, quantification of CLIMP-63 and RTN4 distribution in WT cells. Error bars represent the 95% CI. *C* and *D*, comparison of CLIMP-63 (*C*) and RTN4 (*D*) distribution between WT and RHBDL4 KO HeLa cells. Error bars represent the 95% CI. *E*, rescue of the phenotype. Quantification of CLIMP-63 distribution in RHBDL4 KO cells transiently transfected with HA-tagged RHBDL4 WT or RHBDL4 S144A, *left panel*. Error bars represent the 95% CI. Representative immunofluorescence images from a rescue experiment, *right panel*. *F*, immunofluorescence of CLIMP-63 and RTN4 in WT and RHBDL4 KO cells 24 h after the tunicamycin treatment. *G*, quantification of cells presenting a tunicamycin-induced phenotype. Error bars represent standard deviation (n = 4 experiments, with over 100 cells per experiment analyzed). $p < 0.0001$ *t* test, two-sided (three *asterisks* on the graph) and $p = 0.021$ Mann–Whitney–Wilcoxon test, two-sided. The images and quantifications are representative of at least three independent experiments. In all images, the scale bar represents 10 μm. CLIMP-63, cytoskeleton-linking membrane protein 63; ER, endoplasmic reticulum; HA, hemagglutinin; RTN4, reticulon 4.

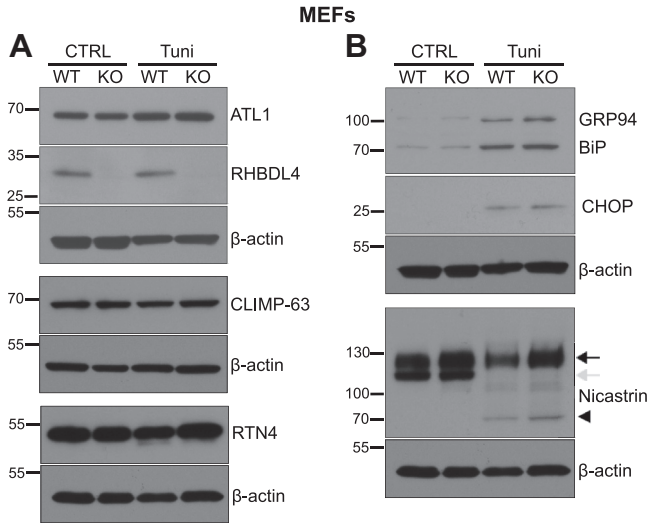

Figure 4. The levels of ER-shaping proteins and the ER stress response are similar in WT and RHBDL4 KO cells. Western blot of total cell lysates from WT and RHBDL4 KO MEFs in control conditions or 24 h after tunicamycin treatment. *A*, Western blots of RHBDL4 and ER-shaping proteins ATL1, CLIMP-63, and RTN4. *B*, Western blots of UPR targets BiP and GRP94 (detected using an anti-KDEL antibody), CHOP, and nicastrin. The *black arrow* represents the mature post-Golgi protein, whereas the *gray arrow* represents the immature ER-localized one. The *arrowhead* represents the nonglycosylated nicastrin, visible in the tunicamycin-treated samples. β-Actin was used as a loading control, and it was developed on the stripped membranes, previously used for detection of the proteins shown above each β-actin panel. RTN and nicastrin Western blots were performed on the same gel and share the same β-actin loading control. The results are representative of three independent experiments. ATL1, atlastin 1; BiP, immunoglobulin binding protein; CLIMP-63, cytoskeleton-linking membrane protein 63; ER, endoplasmic reticulum; GRP94, glucose-regulated protein 94; MEF, mouse embryonic fibroblast; RTN4, reticulon 4; UPR, unfolded protein response.

nicastrin, a component of the γ-secretase complex, which is found in two forms: one immature, ER localized, detected as a lower molecular weight band in Western blots, and one mature, post-Golgi, detected as a higher molecular weight form (45). We found no differences in the levels of post-Golgi nicastrin, either in control or under ER stress conditions (Figs. 4*B* and S4*B*). The efficiency of tunicamycin treatment was similar in the WT and RHBDL4 KO cells, as shown by the appearance of nonglycosylated species of nicastrin. This implies that the overall secretory function of RHBDL4 KO cells is not significantly compromised. Taking all these results together, we conclude that the role of RHBDL4 in shaping the ER under stress conditions is not a secondary effect of a role in homeostasis of ER-shaping proteins, response to ER stress, or general secretion.

RHBDL4 localizes to the ER sheets and interacts with CLIMP-63

The phenotypes we observed so far indicate that RHBDL4 levels have an impact primarily on ER sheets, so we determined the localization of endogenous RHBDL4 within the ER. Several commercial antibodies as well as one produced by our group failed to detect the endogenous RHBDL4 by immunofluorescence. We therefore used a biochemical approach to examine endogenous RHBDL4 localization. We isolated microsomes from mouse liver as well as from HeLa cells and used differential centrifugation to separate the rough and smooth ER on a sucrose cushion (46, 47). As sketched in Figure 5*A*, following ultracentrifugation, the rough ER (R, ER sheets studded with ribosomes) sediments through the 1.3 M sucrose cushion, whereas the smooth ER (S, ER tubules) segregates at the interface between the two sucrose concentrations; the material in between is a rough/smooth, or intermediate (I), ER (5). For HeLa cells, because of a lower amount of material, the smooth ER was not readily visible, and, therefore, we analyzed all fractions starting 1 ml above the interface and finishing with the pellet, as indicated in Figure 5*A* (*right side*).

In agreement with their published localization, we found ATL1 in the smooth ER fraction, RTN4 in both smooth and rough ER, whereas calnexin (CNX)—an ER-resident chaperone—and CLIMP-63 were specific to the rough ER (Fig. 5, *B* and *C*) (4, 48), confirming a good separation. In both, HeLa cells and mouse liver, RHBDL4 distributed predominantly to the rough ER (Fig. 5, *B* and *C*). Upon ER stress, there was no obvious change in RHBDL4 distribution in mouse liver and a somewhat increased level in rough ER in HeLa cells. We obtained similar results in MEFs (Fig. S5). These results show that endogenous RHBDL4 is localized predominantly within the ER sheets, which is consistent with the ER disruption phenotypes we observed.

Next, we asked whether we could detect interactions between RHBDL4 and ER-shaping proteins. In coimmunoprecipitation experiments, we found that endogenous RHBDL4 physically interacts with CLIMP-63 (Fig. 5*D*). Significantly, this interaction had also been found in our previous large-scale interaction screen of the RHBDL4 interactome—CLIMP-63 aka CKAP4 was one of the reproducible hits in HeLa and human embryonic kidney (HEK) 293 cells (49). We could not detect an interaction between RHBDL4 and RTN4, or between RHBDL4 and CNX, another ER sheet membrane protein. The interaction between endogenous RHBDL4 and CLIMP-63 was recapitulated using overexpressed tagged proteins: CLIMP-63 hemagglutinin (HA) pulled down RHBDL4 Myc and, conversely, RHBDL4 HA pulled down CLIMP-63 Myc (Fig. 5*E*, lane 7 and 8, respectively). Both RHBDL4 WT and RHBDL4 S144A coimmunoprecipitated with CLIMP-63 (Fig. 5*F*, lanes 9 and 10), indicating that the interaction with CLIMP-63 did not depend on the RHBDL4 active site.

RHBDL4 associates with the cytoskeleton

CLIMP-63 interacts with microtubules (20), and given the impact of RHBDL4 overexpression and KO on the shape and distribution of the ER, we asked whether RHBDL4 might also interact with the cytoskeleton, which provides a functional scaffold for shaping and distributing the ER.

Using an approach expected to preserve protein–cytoskeleton interactions, we separated the cytoskeletal fraction from HeLa cells (50). During the fractionation, the intermediate filaments and actin cytoskeleton are preserved, as well as the cold-stable microtubules, reported as the ones that interact with other proteins (51) (Fig. 6*A*, the *lower two rows* show actin and tubulin in the soluble [S], nuclear [N], and

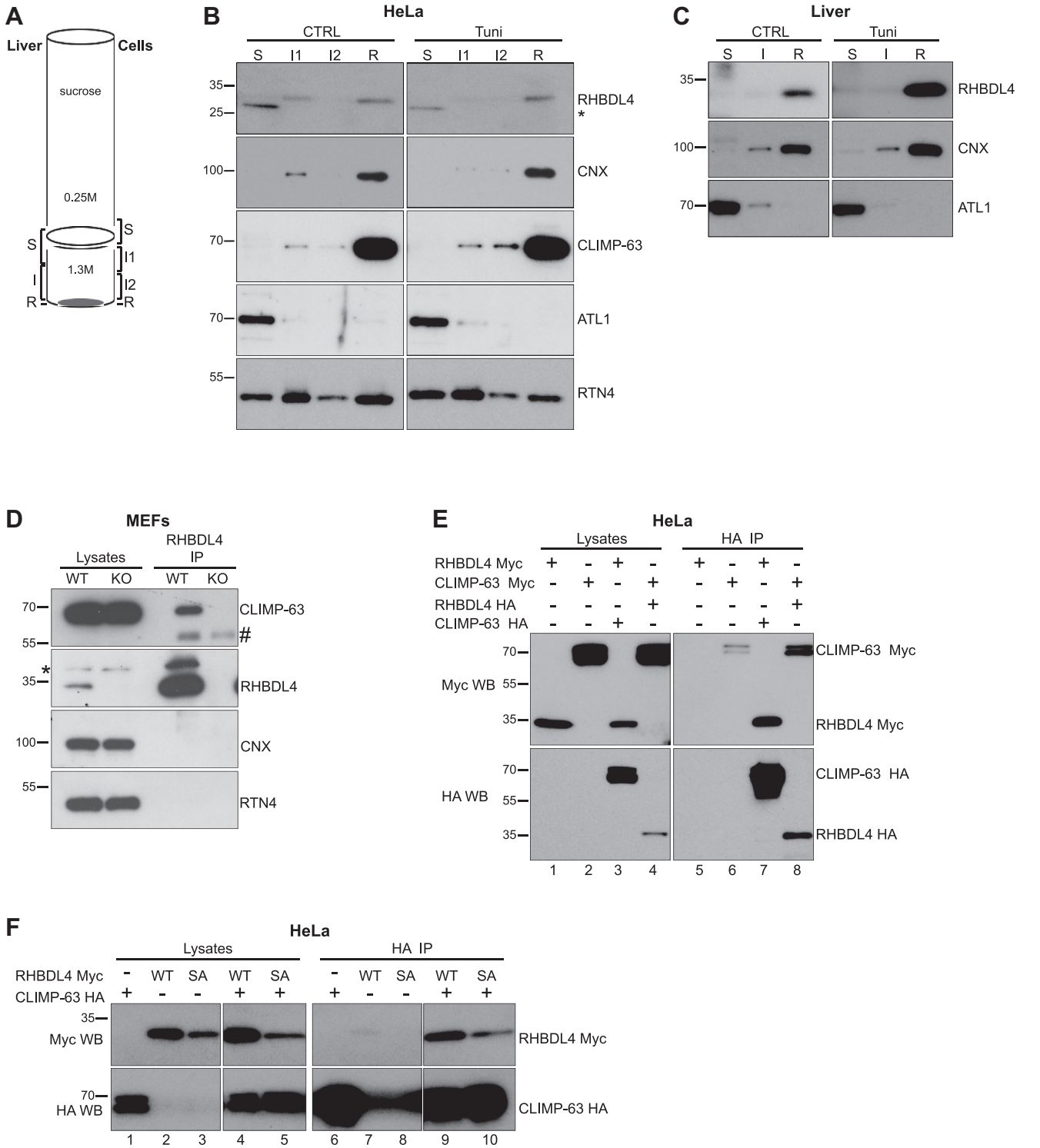

Figure 5. RHBDL4 resides within the ER sheets and interacts with CLIMP-63. *A*, separation of rough and smooth ER by differential centrifugation—schematic representation. *B*, microsomes from HeLa cells, control and tunicamycin treated, were separated as in *A*. Smooth ER (S), rough ER (R), and intermediate ER (I) were analyzed by Western blot for the indicated ER proteins. The *asterisk* represents a nonspecific band. The results are representative of three independent experiments. *C*, microsomes from mouse liver, control, and tunicamycin treated were separated as indicated in *A* and analyzed as in *B*. The results are representative of three mice per condition. *D*, immunoprecipitation of endogenous RHBDL4 followed by Western blot for CLIMP-63 and RHBDL4. The *hash symbol* and the *asterisk* represent immunoglobulin G (IgG) heavy chain and a nonspecific band, respectively. *E*, immunoprecipitation of tagged versions of RHBDL4 WT and CLIMP-63, transiently expressed in HeLa cells, followed by Western blot as indicated. *F*, as in *E*, but including both the WT and S144A (SA) mutant RHBDL4. The results are representative of three independent experiments. ATL1, atlastin 1; CLIMP-63, cytoskeleton-linking membrane protein 63; CNX, calnexin; ER, endoplasmic reticulum; HA, hemagglutinin; RTN4, reticulon 4.

cytoskeletal [C] fractions). Strikingly, most of RHBDL4 and CLIMP-63 segregated into the insoluble cytoskeletal fraction, whereas RTN4 and ATL1 did not (Fig. 6*A*, lane 3). We note that CLIMP-63 segregated almost completely into the cytoskeletal fraction, even though only a small proportion of microtubules were insoluble during the procedure (Fig. 6*A*, lane 3). Although this is not directly relevant to our conclusions, this result suggests that, in addition to its documented interaction with microtubules (20), CLIMP-63 might interact with other components of the cytoskeleton; alternatively, CLIMP-63 may bind preferentially to the cold-stable fraction of microtubules. CLIMP-63 was present in the cytoskeletal fraction independently of RHBDL4 (Fig. 6*A*, lane 6 compared with lane 3). Likewise, when we treated the cells with siRNA against CLIMP-63, RHBDL4 segregated into the cytoskeletal fraction regardless the amounts of CLIMP-63 (Fig. 6*B*, lane 6 compared with lane 3), suggesting that the two proteins associate with the cytoskeleton independently of each other. The cells were treated with CLIMP-63 siRNA and analyzed after 3 days; the efficiency of the siRNA is shown in Figure 6*B* (*lower panel*) in total cell lysates. The cytoskeletal association of RHBDL4 did not depend on its proteolytic activity, as shown by the analysis of transiently expressed HA-RHBDL4 WT and HA-RHBDL4 S144A (Fig. 6*C*, lanes 6 and 9, respectively); to exclude any interference of endogenous RHBDL4, these experiments were done in RHBDL4 KO cells. Similar results were obtained in MEFs (Fig. S6*A*, endogenous RHBDL4, and Fig. S6*B*, transiently expressed HA-RHBDL4 WT and HA-RHBDL4 S144A).

When overexpressed, RHBDL4 disrupted the microtubule organization in a concentration-dependent manner: cells expressing low/moderate levels of RHBDL4 had normal microtubule morphology, whereas cells with higher expression showed dramatically reorganized microtubules (Fig. 7*A*, *second versus third and fourth columns*; the *first column* shows a nontransfected cell). Overexpressing the RHBDL4 S144A mutant showed similar results (Fig. 7*B*).

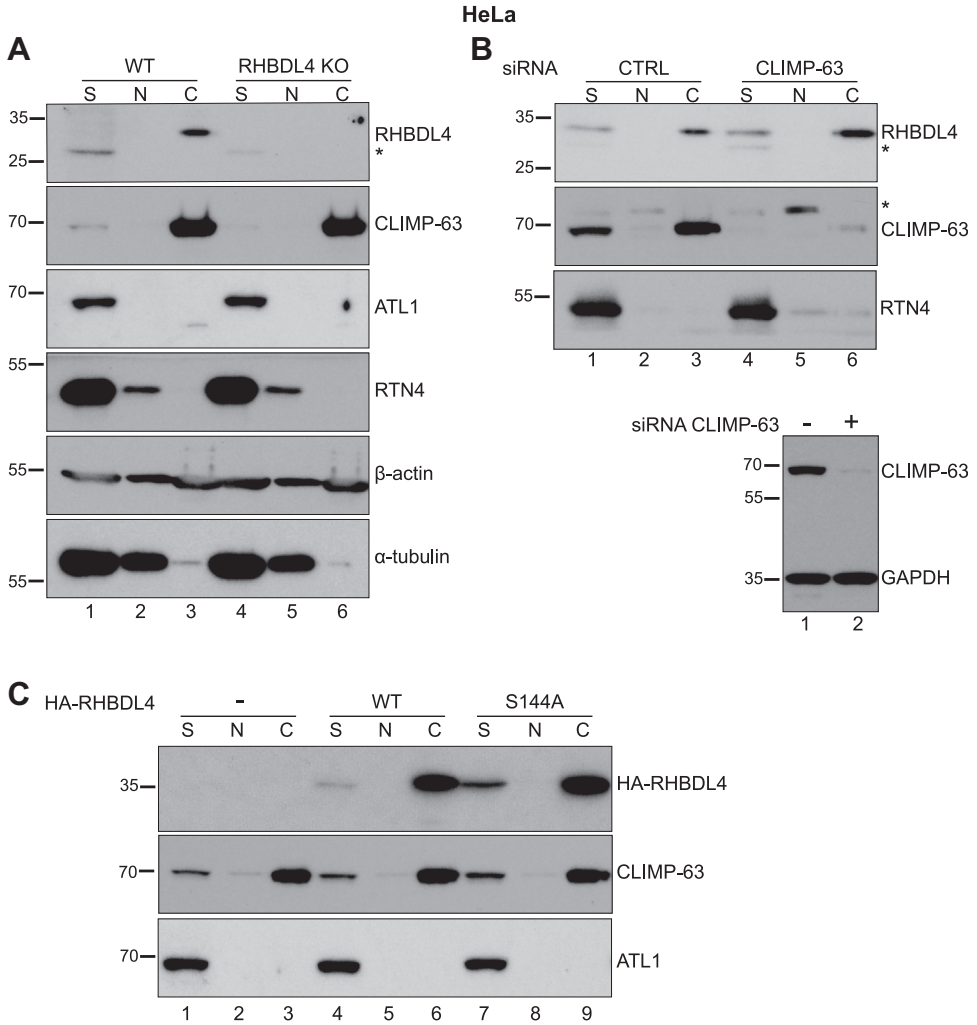

Figure 6. RHBDL4 associates with the cytoskeleton. *A*, Western blot of soluble (S), nuclear (N), and cytoskeletal (C) fractions isolated from WT and RHBDL4 KO HeLa cells and analyzed for ER proteins—RHBDL4, CNX, CLIMP-63, ATL1, RTN4—as well as for β-actin and α-tubulin. *B*, *top panel* as in *A*, Western blot of S, N, and C fractions isolated from HeLa cells treated with CLIMP-63 siRNA 72 h before the analysis. In the *lower panel* are shown the levels of CLIMP-63 in total cell lysates from the same experiment. *C*, anti-HA tag Western blot of C, N, and S fractions isolated from RHBDL4 KO HeLa cells transiently expressing HA-tagged RHBDL4 WT or RHBDL4 S144A. In *A* and *B*, the *asterisk* represents nonspecific bands. The results are representative of three independent experiments. ATL1, atlastin 1; CLIMP-63, cytoskeleton-linking membrane protein 63; CNX, calnexin; ER, endoplasmic reticulum; HA, hemagglutinin; RTN4, reticulon 4.

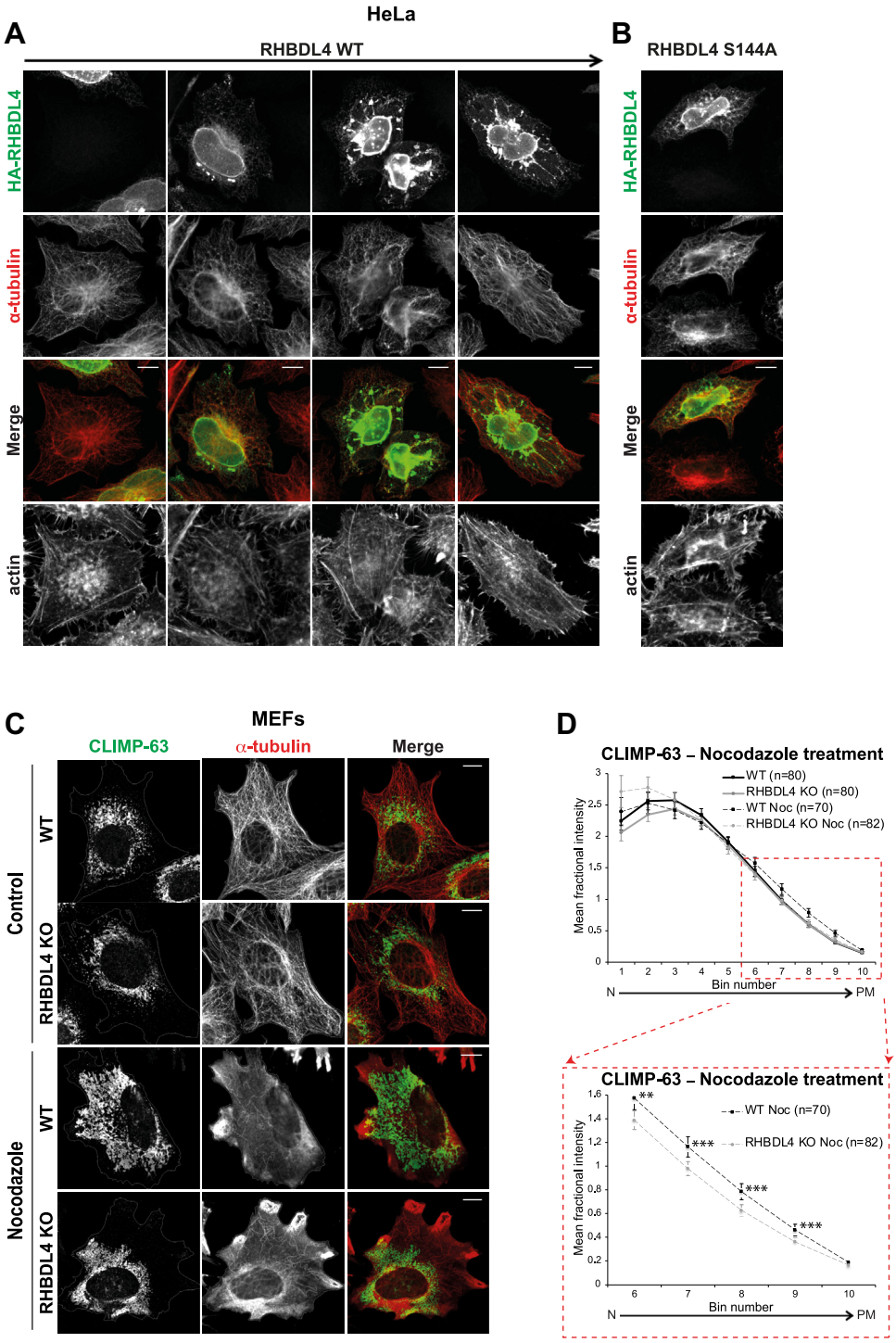

Figure 7. RHBDL4 and microtubules. Immunofluorescence of HeLa cells transiently transfected with HA-tagged RHBDL4 WT in *A* or RHBDL4 S144A in *B*. Cells were stained for HA tag (*green*), α-tubulin (*red*), and actin (*lower row*). The *arrow at the top* indicates increasing expression levels. The images are representative of three independent experiments. *C*, immunofluorescence of WT and RHBDL4 KO MEFs showing the ER sheet (CLIMP-63—*green*) and microtubule (α-tubulin—*red*) distribution under control or nocodazole treatment. *D*, quantification of CLIMP-63 distribution (*upper panel*) and an enlarged area of the graph to emphasize the statistical significance in the peripheral bins (*lower panel*). Error bars represent the 95% CI. $p = 0.0027$ *t* test (two *asterisks* on the graph) and $p = 0.0092$ Mann–Whitney–Wilcoxon test, two-sided, for bin 6; $p = 0.0004$ *t* test (three *asterisks* on the graph) and 0.0029 Mann–Whitney–Wilcoxon test, two-sided, for bin 7; $p = 0.0001$ *t* test (three *asterisks* on the graph) and 0.0003 Mann–Whitney–Wilcoxon test, two-sided, for bin 8; $p = 0.0007$ *t* test (three *asterisks* on the graph) and 0.0015 Mann–Whitney–Wilcoxon test, two-sided for bin 9; $p = 0.0297$ *t* test (one *asterisk* on the graph) and $p = 0.0211$ Mann–Whitney–Wilcoxon test, two-sided for bin 10. The number of cells analyzed is shown on the graph. For *C* and *D*, the results are representative of two independent experiments. In all images, the scale bar represents 10 μm. CLIMP-63, cytoskeleton-linking membrane protein 63; HA, hemagglutinin; MEF, mouse embryonic fibroblast.

RHBDL4 regulates ER sheet morphology

Microtubule depolymerization results in rapid reorganization of the ER network (17, 52, 53). We used this to investigate further a role for RHBDL4 in ER dynamics and distribution in the context of ER–cytoskeleton interaction. We exposed WT and RHBDL4 KO MEFs and HeLa cells to nocodazole, to disrupt the microtubules, and analyzed the resulting changes in ER sheet morphology and distribution. In WT cells, both MEFs and HeLa, the nocodazole treatment led to wide spreading of CLIMP-63 signal throughout the cytoplasm, confirming that the ER sheets underwent a major reorganization (Fig. 7*C*, *third row* and Fig. S7*A*). In RHBDL4 KO, CLIMP-63 redistribution was less pronounced and, in many cells, there were peripheral areas devoid of ER sheets (Fig. 7*C*, *fourth row* and Fig. S7*A*). Quantification of this CLIMP-63 spreading phenotype confirmed the difference in the peripheral distribution between WT and RHBDL4 KO cells (Figs. 7*D* and S7*B*). These results showed that microtubule-dependent ER sheet dynamics are defective in the absence of RHBDL4.

RHBDL4 protects against ER stress in vivo

To study the role of RHBDL4 *in vivo*, we created RHBDL4 KO mice. We detected no obvious phenotype under normal conditions, but the fact that RHBDL4 KO MEFs only showed a phenotype when challenged with tunicamycin (or nocodazole) prompted us to examine the effect of ER stress in KO mice.

We used intraperitoneal injection of a sublethal dose of tunicamycin (1 μg/g body weight) (54, 55) to induce ER stress and followed the mice over 3 days. The first difference we noticed between WT and RHBDL4 KO mice was in weight loss: at day 3 of the treatment, the RHBDL4 KO mice had lost significantly more weight than WT animals (Fig. 8*A*), suggesting that the former were more severely affected by induced ER stress. Liver is the mouse tissue with the strongest response to tunicamycin-induced ER stress (56) and one of the tissues with high RHBDL4 expression (Fig. 8*B*). We therefore looked for further phenotypic differences between the livers of tunicamycin-treated WT and RHBDL4 KO mice. Upon dissection, we noticed a striking difference at 3 days of treatment, with the latter being pale in color, a sign of liver steatosis. Oil Red O (ORO) staining of liver sections confirmed this; after 3 days of treatment, the RHBDL4 KO mice accumulated dramatically elevated levels of neutral lipids in their livers when compared with WT (Fig. 8*C*). At day 1, there was no apparent difference between the two genotypes (Fig. S8*A*).

To check whether the failure of RHBDL4 KO mice to cope with ER stress induced by tunicamycin was due to a deficient activation of the UPR, we measured the upregulation of UPR targets BiP and GRP94, as well as another marker of UPR activation, the splicing of X-box binding protein-1 (XBP1). In response to ER stress, XBP1 mRNA undergoes splicing and is translated into an active transcription factor. The transcriptional program triggered by XBP1 leads to ER expansion as well as upregulation of ERAD and secretory pathway components (57). We found no differences between WT and RHBDL4 KO mice (Fig. 8*D*, quantified in Fig. S8*B*), indicating that RHBDL4 KO mice do not have a defect in UPR activation. Nevertheless, 3 days after tunicamycin treatment, the ER stress was unresolved in RHBDL4 KO mice, as indicated by the persistence of the proapoptotic transcription factor CHOP (Fig. 8*E*, quantified in Fig. S8*C*). RHBDL4 expression itself was upregulated by the tunicamycin treatment, consistent with a role for it in coping with ER stress (Fig. 8*F*).

For a better insight into the phenotype of RHBDL4 KO mice under ER stress, we performed transmission electron microscopy (TEM) on liver sections and looked at the appearance of the ER. Under control conditions, the ER looked similar in WT and RHBDL4 KO livers, with stacks of rough ER packed around the mitochondria (Fig. 8*G*, *left column*, *blue arrows*). Twenty-four hours after tunicamycin treatment, in both genotypes, the rough ER lost the appearance of organized stacks, became dilated, and distributed broadly throughout the cytoplasm, with only scarce ER sheets around mitochondria (Fig. 8*G*, *middle column*). By 72 h after tunicamycin treatment, in WT livers, the ER had started to recover into structures of stacks around the mitochondria, whereas in RHBDL4 KO, the rough ER remained dilated, filling the cytoplasm; there was also an accumulation of large lipid droplets (LDs) (Fig. 8*G*, *right column*). We quantified this ER phenotype by measuring the luminal width of the gap between the two sides of the ER sheets and found that at 24 h after tunicamycin treatment, the ER sheets in RHBDL4 KO livers were modestly but significantly narrower than in the WT (Fig. 8*H*). As obvious from visual inspection, the WT ER sheets decreased in luminal width between 24 and 72 h after tunicamycin treatment, indicating a recovery from ER stress; in contrast, the ER sheets had become even more dilated in the RHBDL4 KO livers (Fig. 8*H*). These data demonstrate that in RHBDL4 KO livers, there is a defect in the dynamics of ER sheets under ER stress and further indicate a defect in the resolution of ER stress in the absence of RHBDL4.

Discussion

In metazoans, the ER has a complex architecture with different ER morphologies hosting different functions. The ER architecture differs between cell types and undergoes changes during the cell cycle and according to physiological needs. There is significant knowledge about how the ER tubules are generated and maintained but not as much is known about the ER sheets. How do rapid changes in shape and distribution of the organelle take place, and what are the regulators? What factors contribute to the positioning of the ER within the cell, and how does the ER interact with the cytoskeleton? We report here that RHBDL4 plays a role in ER sheet dynamics during ER stress, that it interacts with CLIMP-63 and the cytoskeleton, and that it is essential for coping with ER stress in mice.

We have shown that endogenous RHBDL4 resides primarily within the ER sheets. Consistent with this, the phenotypes induced by its overexpression or KO were mostly at the level of ER sheets, especially during conditions that require their reorganization/redistribution—ER stress or microtubule depolymerization. In response to ER stress, mammalian and

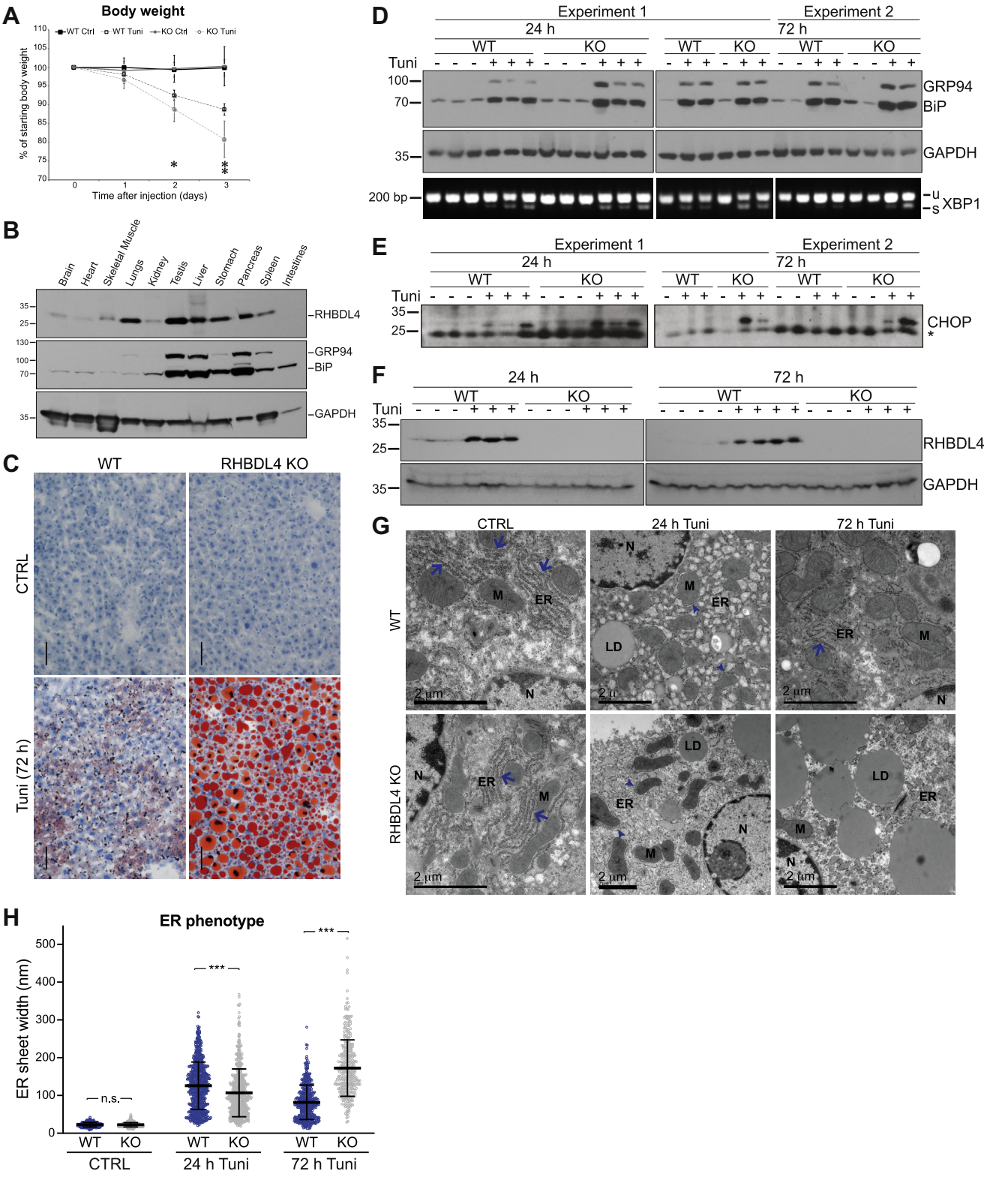

Figure 8. RHBDL4 protects against the ER stress in mice. *A*, body weight changes of WT and RHBDL4 KO mice control or treated with tunicamycin. Errors bars represent 95% CI (six to eight mice per genotype per condition, combined from three different experiments). The *asterisks* represent the statistical significance for WT Tuni *versus* RHBDL4 KO Tuni: day 1, $p = 0.3324$, *t* test, two-sided, and $p = 0.4875$ Mann–Whitney–Wilcoxon test, two-sided; day 2, $p = 0.0230$, *t* test, two-sided (one *asterisk* on the graph), and $p = 0.0151$ Mann–Whitney–Wilcoxon test, two-sided; day 3 $p = 0.0014$ *t* test, two-sided (two *asterisks* on the graph), and $p = 0.0151$ Mann–Whitney–Wilcoxon test, two-sided. *B*, Western blot for RHBDL4 in mouse liver lysates from WT mice. BiP and GRP94 (detected using an anti-KDEL antibody) were used as ER markers, and GAPDH was used as a loading control. *C*, Oil Red O staining of liver tissue sections from WT and RHBDL4 KO mice, control or 72 h after tunicamycin treatment. The scale bar represents 50 µm. The results are representative of two experiments with a total of four to six mice per genotype per condition. *D*, Western blot for BiP and GRP94 (detected using an anti-KDEL antibody) in mouse liver lysates from WT and RHBDL4 KO mice, control, or tunicamycin treated for the indicated times (*top panels*). GAPDH was used as loading control. The *lower panels* show the corresponding XBP1 splicing, examined by RT–PCR using primers flanking the intron region. *E*, Western blot for CHOP. The *asterisk*

yeast ER undergoes significant changes in size, morphology, and distribution (27, 28, 57). In both cell lines we used in this study, human HeLa cells and MEFs, RHBDL4 KO led to defective redistribution of ER sheets. At the same time, the function of the ER, in terms of secretion, and the activation of the UPR were similar in WT and RHBDL4 KO cells, suggesting that RHBDL4 participates in adapting ER shape to the cellular context, rather than in ER function. Overall, the common theme that emerges from our results is that RHBDL4 has a role in ER sheet dynamics; in its absence, the ER sheets were more compact around the nucleus and more stable to disassembly and redistribution, whereas moderate overexpression had the opposite effect.

The reticular network of ER tubules can be reconstituted *in vitro* using a small number of proteins—RTNs, REEPs, and ATLs (10, 11)—but the ER sheets have a more complex structure, and it is not clear how they are generated and maintained. None of the components shown to stabilize ER sheets are essential and, even though there are indications that the ER sheets interact with both microtubules and the actin cytoskeleton (15, 20), the actual mechanisms involved in their dynamics and positioning are poorly understood. We found an interaction between RHBDL4 and the ER sheet protein CLIMP-63. Our fractionation experiments demonstrated that both proteins segregated into the cytoskeleton-binding fraction, although it is important to note that their interaction with the cytoskeleton was independent of each other, suggesting that RHBDL4 associates with the cytoskeleton either directly or *via* a different intermediate. Overexpression of RHBDL4 disrupted microtubule organization suggesting a functional relationship, but the effect was different to that reported for CLIMP-63. When overexpressed, CLIMP-63 coaligns with microtubules, and together they form bundles around the nucleus (20). CLIMP-63 forms homo-oligomers *via* its luminal domain, which limit its movement within the plane of membrane (58), and it is thought to form intermembrane bridges to stabilize the ER sheets (4, 59). One possibility is that RHBDL4 interferes with the formation of CLIMP-63 homo-oligomers or intraluminal bridges to allow ER sheets to be dynamic when needed. We emphasize that this is a speculative idea at this stage, but overall our data suggest that, while CLIMP-63 plays a structural role in ER sheets, RHBDL4 appears to be involved in their dynamics, playing a regulatory role.

To date, there is no reported substrate for RHBDL4 that could explain this role, and none of the ER-shaping proteins we checked appeared to be cleaved by RHBDL4. Indeed, the effects we describe here using overexpression were similar for RHBDL4 WT and the catalytically inactive mutant RHBDL4 S144A: the effect on ER and microtubules, the segregation into the cytoskeletal fraction, and the interaction with CLIMP-63. Moreover, both RHBDL4 WT and RHBDL4 S144A rescued partially the phenotype in RHBDL4 KO HeLa in control conditions. This leads us to conclude that the function we describe in ER shape and dynamics is independent of the catalytic function of this rhomboid protease. This conclusion is made more complex by the fact that expression of RHBDL4 S144A induces ER stress, making the interpretation of some experiments difficult. Even though we used low expression levels for rescue experiments, the ER stress induced by expressing the mutant can mask a rescue of RHBDL4 function. Nevertheless, the balance of all the evidence in both cell types suggests a nonproteolytic function for RHBDL4 in this context. To our knowledge, this is the first report of a nonproteolytic function for a functional secretase rhomboid (*i.e.*, not an iRhom or other more distant member of the rhomboid-like superfamily (60)); however, it is not new in the world of enzymes. Among enzymes shown to fulfill additional noncatalytic functions are kinases, matrix metalloproteinases, and presenilins, and the noncatalytic functions of these enzymes range from scaffolding to protein trafficking and calcium signaling (61–64).

Pharmacological ER stress induces transient LD accumulation in mouse liver and, when combined with a defective UPR signaling, it leads to hepatic steatosis. Genetic disruption of any of the three UPR branches or of protein quality control results in failure to cope with the ER stress and hepatic steatosis (28, 55), most likely caused by a failure to upregulate the necessary folding machinery. When challenged with tunicamycin, RHBDL4 KO mice showed a phenotype similar to that described for UPR-deficient mice: significant weight loss and liver steatosis, characterized by massive accumulation of LDs. However, in RHBDL4 KO mice, UPR activation was normal (as shown by XBP1 splicing, and BiP and GRP94 upregulation), suggesting a different cause for the failure to cope with the ER stress. Three days after tunicamycin treatment, in WT livers, ER sheets began to reassemble around the mitochondria, whereas in RHBDL4 KO livers, the ER remained dilated and scattered through the cytoplasm, and large LDs were common. Although ER stress results in LD accumulation, and the disruption of LD biogenesis induces the UPR (65), the role of LDs in the ER stress response remains unclear. Our data further emphasize the relationship between ER stress and LD accumulation, but further work is needed to uncover the factors and mechanisms involved in ER sheet reassembly and LD

represents a nonspecific band that serves as a loading control. *F*, Western blot as in *D*, but for RHBDL4. *G*, electron microscopy of liver tissue sections from WT and RHBDL4 KO mice, control, 24 or 72 h after tunicamycin treatment. The *blue arrows* indicate stacked ER sheets; the *arrowheads* indicate remainder nondilated ER sheets in tunicamycin-treated samples. The results are representative of at least three mice per genotype per condition. *H*, quantification of ER phenotype presented in *G*. The luminal width of ER sheet structures from TEM images of liver tissue sections from WT and RHBDL4 KO mice, control, 24 or 72 h after tunicamycin treatment (from experiment 1 presented in *D* and *E*) was measured. Two or three mice per genotype per condition were analyzed, with five to eight cells per mouse, and between 11 and 80 measurements per cell. The data points on the graph represent one measurement each. Errors bars represent standard deviation. The *asterisks* represent the statistical significance: WT CTRL *versus* RHBDL4 KO CTRL, $p = 0.6273$ (n.s.) *t* test, two-sided, and $p = 0.4285$ Mann–Whitney–Wilcoxon test, two-sided; WT Tuni *versus* RHBDL4 KO Tuni, 24 h, $p < 0.001$ (three *asterisks* on the graph) *t* test, two-sided, and $p < 0.001$ Mann–Whitney–Wilcoxon test, two-sided; WT Tuni *versus* RHBDL4 KO Tuni, 72 h $p < 0.001$ (three *asterisks* on the graph) *t* test, two-sided, and $p < 0.001$ Mann–Whitney–Wilcoxon test, two-sided. BiP, immunoglobulin binding protein; ER, endoplasmic reticulum; GRP94, glucose-regulated protein 94; LD, lipid droplet; M, mitochondria; N, nucleus; n.s., not significant; TEM, transmission electron microscopy; XBP1, X-box binding protein-1.

clearing after ER stress: our work suggests that RHBDL4 participates in this stress resolution. Notably, some proteins with well-defined roles in ER shape—for example, ATL, REEP1, and spastin—are known to affect LD biology (66–68), but none of these roles have been studied in the context of ER stress.

In conclusion, while the relevant molecular and cellular mechanisms remain to be discovered, we have uncovered a physiological role for RHBDL4 in regulating the morphology and distribution of ER sheets. Our work has also shown that this previously unrecognized RHBDL4 function is essential in cells for coping with conditions that require dynamic reorganization of ER sheets and in mice for resolving the pathology associated with ER stress.

Experimental procedures

Cell culture, DNA constructs, and transfections

MEFs and HeLa cells (WT and RHBDL4 KO) were cultured in Dulbecco's modified Eagle's medium (DMEM) supplemented with 10% heat-inactivated fetal bovine serum and penicillin–streptomycin, at 37 °C in 5% CO_2. The triple HA-tagged RHBDL4 construct in pcDNA3.1 plasmid has been described previously (33). Using an untagged version of this plasmid, a C-terminal Myc tag was inserted using site-directed mutagenesis. CLIMP-63 complementary DNA (cDNA) was purchased from Open Biosystems (MHS6278-202833153), subcloned into pcDNA3.1, and HA or Myc tag was added by site-directed mutagenesis. All constructs were validated by sequencing. For overexpression and rescue experiments, 60 to 70% confluent cells were transfected with the cDNA of interest in pcDNA3.1 plasmid. Polyethylenimine (PEI; 25 kDa linear; Polysciences)-mediated transfections were carried out using a DNA to PEI ratio of 1:2.5 (w/w), in complete medium, for HeLa cells. For MEFs, a DNA to PEI ratio of 1:3 (w/w) was used, and the transfections were done in serum-free medium for 5 h, after which the transfection medium was replaced with complete fresh DMEM. The cells were analyzed 24 h after transfection.

Generation of MEFs

Embryonic fibroblasts were generated from RHBDL4 WT and RHBDL4 KO E14.5 embryos and immortalized using lentiviral transduction of SV40 virus large T antigen (Ef1a_Large T-antigen_Ires_Puro; Addgene plasmid 18922), as described by Christova *et al.* (69).

RHBDL4 KO HeLa cells

The RHBDL4 KO HeLa cells were generated using the CRISPR/Cas9 system. The guide RNAs (gRNAs) were designed online (http://www.e-crisp.org/) (70). Four different gRNAs were cloned into pSpCas9(BB)-2A-Puro (PX459) plasmid (71) and tested in HeLa cells. The cells were transfected with PX459 plasmid containing the gRNAs and, 48 h after transfection, the cells were treated with puromycin to select the transfectants. The levels of RHBDL4 were assessed by Western blot, and the most efficient gRNA (TAGTGTGG AGAAGTGTTACC, targeting the first coding exon) was selected for further use in this study. Single-cell clones transfected with the aforementioned gRNA were selected and used.

U2OS Flp-In stable cell lines

U2OS Flp-In stable cell lines expressing N-terminal triple HA-tagged RHBDL4 (WT or S144A) were obtained by cotransfecting the pcDNA5/FRT vector containing the cDNA for RHBDL4 and the pOG44 plasmid at a ratio of 1:9. Stably transfected cells were selected and maintained in DMEM supplemented with 10% fetal bovine serum and 200 μg/ml hygromycin. To induce the expression of RHBDL4, ∼70% confluent cells were treated with tetracycline and analyzed by Western blot 24 h later.

Tunicamycin and nocodazole treatment

To induce ER stress, the cell culture medium of ∼70% confluent cells was replaced with fresh medium containing tunicamycin (0.1 μg/ml for MEFs and 5 μg/ml for HeLa, final concentration; product no.: T7765; Sigma–Aldrich), and the cells were incubated at 37 °C, 5% CO_2, for 24 h. For rescue experiments, MEF cells were transfected in serum-free medium for 5 h (as described previously) after which the transfection medium was replaced with complete fresh medium containing tunicamycin. The cells were analyzed 24 h after treatment. For microtubule depolymerization experiments, the cell culture medium of ∼70% confluent cells was replaced with fresh medium containing 10 μM nocodazole (catalog no.: M1404; Sigma–Aldrich), and cells were incubated at 37 °C, 5% CO_2, for 15 min. In both cases, control cells were treated with dimethyl sulfoxide.

Immunoprecipitation

All experiments were performed on ∼80% confluent cells. For endogenous RHBDL4, the immunoprecipitation was done using the Pierce Crosslink Magnetic IP/Co-IP Kit (catalog no.: 88805; Thermo Fisher Scientific), according to the manufacturer's protocol. The cells were washed twice with ice-cold PBS and lysed in lysis buffer (25 mM Tris, 150 mM NaCl, 1 mM EDTA, 1% NP-40, 5% glycerol, and pH 7.4) containing EDTA-free protease inhibitor cocktail (catalog no.: 11873580001; Roche). Lysates were centrifuged at 10,000*g* for 10 min, and the postnuclear supernatants were used for subsequent immunoprecipitation. Cell lysates were incubated with a rabbit anti-RHBDL4 antibody, described by Fleig *et al.* (29), cross-linked to Protein A/G magnetic beads, for 1 h at 4 °C on a rotator. Immunoprecipitates were washed three times with lysis buffer and eluted with the included elution buffer (pH 2.0). The eluates were neutralized, mixed with 5× sample buffer including 50 mM DTT, and incubated at 65 °C for 10 min prior loading onto gels. Cell lysates were prepared with 5× sample buffer and DTT and incubated at 65 °C, alongside the eluates. Samples were analyzed by SDS-PAGE (Novex; WedgeWell 8–16% Tris–glycine mini gels) followed by Western blot. For overexpressed RHBDL4 and CLIMP-63, immunoprecipitation was done similarly to the previously

mentioned one, except the lysis buffer contained CHAPS instead of NP-40, and anti-HA or anti-Myc magnetic beads were used.

Cytoskeleton enrichment

The cytoskeletal fraction was separated using the ProteoExtract Cytoskeleton Enrichment and Isolation Kit (catalog no.: 17-10195; Millipore), following the manufacturer's protocol. The experiments were performed on 80 to 90% confluent cells. At the end of collection, the soluble, nuclear, and cytoskeletal fractions were adjusted to equal volumes and mixed with 5× SDS-PAGE sample buffer and 50 nM DTT. The samples were incubated at 65 °C for 10 min, and equal volumes were loaded onto gels (WedgeWell 8–16% Tris–glycine mini gels) and analyzed by Western blot.

Microsome separation and ER fractionation

Microsomes were separated from MEFs, HeLa cells, or mouse liver using the protocol described by Song *et al.* (47), adapted. All steps of the protocol were performed on ice, and all solutions contained protease inhibitor cocktail. The livers from sacrificed animals were rapidly removed and placed in ice-cold PBS. After three washes with PBS, the livers were cut into pieces and weighed. Small pieces (1–3 mm^3) were mixed with five volumes (w/v) of homogenization solution (0.25 M sucrose; 10 mM Hepes; pH 7.5) and homogenized by five manual strokes using a Dounce tissue grinder and loose-fitting pestle. The homogenates were centrifuged at 1000*g*, 4 °C, for 10 min. The supernatants were collected and centrifuged at 8,000*g*, 4 °C, for 15 min. The supernatants were diluted with homogenization solution and 15 mM CsCl to a total volume of 6 ml and laid gently on a cushion of 1.3 M sucrose, 10 mM Hepes, 15 mM CsCl, pH 7.5, and centrifuged at 200,000*g* for 2 h, at 4 °C. One milliliter fractions starting from the interface (0.25 M/1.3 M sucrose) were collected. The pellet was solubilized in 1 ml of 0.25 M sucrose, 10 mM Hepes, 15 mM CsCl, and pH 7.5. The fractions were mixed with 5× SDS-PAGE sample buffer and 50 mM DTT and incubated at 65 °C for 10 min. Equal volumes were loaded onto gels (WedgeWell 8–16% Tris–glycine mini gels) and analyzed by Western blot.

Microsome separation from cells was done using the same protocol, except the homogenization was done using the tight-fitting pestle and 25 strokes, and the fractions were collected starting 1 ml above the interface. For each sample, three 10 cm dishes of 80 to 90% confluent cells were used. The cells were washed one time with ice-cold PBS and one time with homogenization buffer before being scraped in homogenization buffer and transferred to the Dounce tissue grinder.

Western blot

For Figures 4 and S4, the cells were lysed in ice-cold radioimmunoprecipitation assay buffer (RIPA) (150 mM sodium chloride, Triton X-100, 0.5% sodium deoxycholate, 0.1% SDS, 50 mM Tris, and pH 8.0), containing EDTA-free protease inhibitor cocktail and Benzonase (catalog no.: E1014-5KU; Sigma–Aldrich), after which the lysates were mixed with 5× sample buffer and 50 mM DTT. The whole cell lysates were incubated at 65 °C for 10 min prior loading onto gels (WedgeWell 8–16% Tris–glycine mini gels). For Western blot analysis of mouse tissues, small pieces of tissues were homogenized in RIPA buffer supplemented with protease inhibitor cocktail, using a handheld tissue homogenizer. The homogenates were centrifuged at 10,000*g* for 15 min, and supernatants were mixed with 5× sample buffer and 50 mM DTT and incubated at 65 °C for 10 min prior loading onto gels (WedgeWell 8–16% Tris–glycine mini gels). For all other experiments, the sample preparation is described in the corresponding Experimental procedures section. After electrophoresis, the proteins were transferred to polyvinylidene difluoride membrane (Millipore). Membranes were blocked in 5% low-fat milk in PBS and then incubated with primary antibodies in 0.1% Tween–PBS at 4 °C overnight, for anti-CHOP, or at room temperature for 1 h, for the rest of the antibodies. After three washes, membranes were incubated with the appropriate horseradish peroxidase (HRP)–conjugated secondary antibodies for 30 min and washed three times. Antibodies were visualized using Amersham ECL detection reagent (catalog no.: RPN2209) and X-ray films. The following primary and secondary antibodies were used: rabbit polyclonal anti-RHBDL4 obtained as described by Fleig *et al.* (29), rat monoclonal anti-HA-HRP (Roche; catalog no.: 12 013 819 001), mouse monoclonal anti-beta-actin-HRP (Sigma–Aldrich; catalog no.: A3854), rabbit anti-ATL1 (Santa Cruz; catalog no.: sc-67232), mouse anti-RTN4 (Nogo, Santa Cruz; catalog no.: sc-271878), mouse anti-KDEL (Abcam; catalog no.: ab12223), mouse anti–alpha-Tubulin (Abcam; catalog no.: ab-7291), rabbit anti-CLIMP-63 (CKAP4; Proteintech; catalog no.: 16686-1-AP), goat anti-Nicastrin (Santa Cruz; catalog no.: sc-14369), mouse anti-CHOP (Cell Signalling; catalog no.: 2895), rabbit anti-CNX (Santa Cruz; catalog no.: sc-11397), goat anti-Myc-HRP (Abcam; catalog no.: ab1261), mouse anti-GAPDH (Sigma; catalog no.: G8795), mouse antivimentin (kit #17-10195; Millipore), goat polyclonal anti-rabbit-HRP (Bio-Rad; catalog no.: 170-6515), mouse monoclonal antigoat-HRP (Santa Cruz; catalog no.: sc-2354) or goat polyclonal antimouse-HRP (Santa Cruz; catalog no.: sc-2055). Western blot quantification was done using the Gel Analysis tool in Fiji (72).

Immunofluorescence

For immunofluorescence, HeLa and MEF cells were grown in 8-well culture slides uncoated or coated with poly-D-lysine, respectively (Falcon [catalog no.: 354108] and Corning BioCoat [catalog no.: 354632]). Before staining, cells were washed twice with PBS, fixed with 4% paraformaldehyde (Electron Microscopy Sciences) in PBS for 20 min, permeabilized with 0.2% Triton X-100 in PBS for 5 min, and blocked with 1% bovine serum albumin in PBS for 30 min. Cells were incubated with primary antibodies for 1 h and with secondary antibodies for 30 min, both in blocking buffer. Every step of the

aforementioned protocol was followed by three PBS washes. Primary antibodies used for staining were rat anti-HA (Roche; catalog no.: 11867 423 001); rabbit anti-CLIMP-63 (CKAP4; Proteintech; catalog no.: 16686-1-AP), goat anti-RTN4 (Nogo; Santa Cruz; catalog no.: sc-11027), mouse anti-alpha-Tubulin (Abcam; catalog no.: ab-7291). The fluorophore-conjugated secondary antibodies Alexa Fluor 488, Alexa Fluor 568, and Alexa Fluor 647 donkey antimouse, donkey anti-rabbit, and donkey antigoat (all from Invitrogen) were used in various combinations. For actin detection, Alexa Fluor 568 or Alexa Fluor 647 Phalloidin was used. After the last PBS wash, the chamber slides were disassembled, and coverslips were mounted on top of the cells using Fluoromount-G mounting solution containing 4′,6-diamidino-2-phenylindole (Southern Biotech). Single-slice images were taken on a Zeiss 880 microscope using the confocal settings.

Image analysis and quantification

For figures, the brightness/contrast of images were adjusted in Fiji (72), using the same settings across images belonging to the same experiment. Quantification of signal intensity was done using CellProfiler-3.0.0 (39). The area between the nucleus and plasma membrane was divided into 10 bins, and the mean fractional intensity at a given radius was calculated as fraction of total intensity normalized by the fraction of pixels at that radius. For cell segmentation, the nuclei were used as primary objects, and merged images of phalloidin or tubulin (for whole-cell staining) and CLIMP-63 (ER staining) were used to identify the whole cell area. The cells that were not segmented correctly were manually removed from the analysis.

RT–PCR

To detect the XBP1 splicing, the RNA from mouse liver was isolated using RNeasy Mini Kit (Qiagen; catalog no.: 74104) according to the manufacturer's instructions. RT–PCR was performed using 0.5 μg total RNA per reaction, 0.6 μM each XBP1-specific primers, and one-step RT–PCR (QIAGEN OneStep RT–PCR; catalog no.: 210212). The PCR products were analyzed by 2% agarose gel. The primers used were 5′-gaagagaaccacaaactcca-3' (forward) and 5′-ggatatcagactcagaatct-3' (reverse).

Mice

RHBDL4 KO mice were obtained using the Cre-loxP system. Briefly, the targeting construct contained the floxed exon 2 (the first coding exon, encoding the first 144 amino acids, including the catalytic serine) of RHBDL4. The loxP sites were introduced by recombineering, and the successful targeting of EK.CCE embryonic stem (ES) cells was confirmed by Southern blotting (73). Exon 2 was excised in the targeted ES cells by expressing Cre recombinase. Two independent clones of targeted ES cells with excised exon 2 were injected into blastocysts derived from C57BL6 mice and implanted into pseudopregnant female Institute of Cancer Research mice using standard techniques. The resulting chimeric mice were crossed to WT mice to confirm the germline transmission and to further obtain homozygous RHBDL4$^{-/-}$ mice in the next generation. Genotyping was performed by PCR, and the mice were age and sex matched for experiments.

For tunicamycin-induced ER stress, mice between 9 and 14 weeks old were used across experiments. Tunicamycin stock solution was dissolved in dimethyl sulfoxide and diluted 100× in 150 mM sucrose prior injection. One intraperitoneal injection of tunicamycin (1 μg/g body weight) or vehicle was administered, and the mice were followed over the indicated times. Mice were housed in temperature-controlled conditions with a 12 h light–dark cycle and fed on standard rodent chow. All procedures were conducted under a Project Licence (PPL 80/2584) approved by the UK Home Office and the Dunn School of Pathology Animal Welfare and Ethics Review Board.

Mouse liver histology

For TEM, small pieces of liver (1–2 mm^3) from sacrificed animals were rapidly collected and transferred to fixative solution (4% paraformaldehyde + 2.5% glutaraldehyde in 0.1 M Pipes [pH 7.2]) and stored at 4 °C overnight before processing. A Leica EM TP automated processing unit was used for sample processing. Samples were washed three times in 0.1 M Pipes buffer, one time in 0.1 M Pipes containing 50 nM glycine to block free aldehydes, followed by a final wash in 0.1 M Pipes. Samples were stained with 1% osmium tetroxide in 0.1 M Pipes for 2 h at 4 °C and subsequently washed four times with water and stained with 0.5% uranyl acetate at 4 °C for approximately 12 h. After two washes with water, the samples were taken through a dehydration series of 30, 50, 70, 90, and 95% ethanol, 15 min each, at room temperature, and three incubations in 100% ethanol, 30 min each. The samples were infiltrated with TAAB low-viscosity epoxy resin as it follows: 25% resin in ethanol for 1 h, 50% resin in ethanol for 3 h, 75% resin in ethanol for 2 h, then nine times in 100% resin, 5 h each. Samples were removed from the tissue processor and placed in Beem capsule molds containing fresh resin and polymerized at 60 °C for 48 h. Ultrathin (90 nm) resin sections were obtained using a Diatome diamond knife with a Leica UC7 ultramicrotome and transferred to 200 mesh copper grids. The grids were poststained for 5 min with Reynold's lead citrate and imaged using a Gatan OneView camera in an FEI Tecnai 12 TEM operated at 120 kV.

The luminal width of ER sheet structures was measured using ImageJ. One image per cell was analyzed, and all identified ER sheet structures were measured.

For ORO staining, fresh liver pieces were collected in optimal cutting temperature compound in cryomolds and frozen on dry ice. Cryosections, 10 μm thick, were stained with ORO and imaged on a COOLSCOPE slide scanner (Nikon).

Statistical analysis

The statistical significance was obtained using two-sided *t* test and two-sided Mann–Whitney–Wilcoxon test.

Data availability

All data associated with this work are included within the article and supporting figures.

Supporting information—This article contains supporting information.

Acknowledgments—We thank Sonia Muliyil for critical reading of the article. We thank Yonka Christova for generating the KO mice and MEFs; Pedro Carvalho for the gift of U2OS Tet-On cells; Errin Johnson and Anna Pielach (Dunn School EM Facility) for the EM; and Richard Stillion for the ORO staining. Confocal microscopy imaging was done at the Dunn School Bioimaging Facility (Micron Advanced Bioimaging Unit).

Author contributions—V. L. L. and M. F. conceptualization; V. L. L. and C. L. investigation; V. L. L. writing–original draft; V. L. L. and M. F. writing–review & editing; M. F. funding acquisition.

Funding and additional information—This work was supported by Wellcome Trust, United Kingdom Investigator Awards to M.F. (grant nos.: 101035/Z/13/Z and 220887/Z/20/Z).

Conflict of interest—The authors declare that they have no conflicts of interest with the contents of this article.

Abbreviations—The abbreviations used are: ATL, atlastin; BiP, immunoglobulin binding protein; cDNA, complementary DNA; CHOP, C/EBP homologous protein; CLIMP-63, cytoskeleton-linking membrane protein 63; CNX, calnexin; DMEM, Dulbecco's modified Eagle's medium; ER, endoplasmic reticulum; ERAD, ER-associated protein degradation; ES, embryonic stem; GAPDH, Glyceraldehyde-3-phosphate dehydrogenase; gRNA, guide RNA; GRP94, glucose-regulated protein 94; HA, hemagglutinin; HRP, horseradish peroxidase; LD, lipid droplet; MEF, mouse embryonic fibroblast; ORO, Oil Red O; PEI, polyethylenimine; REEP, receptor expression–enhancing protein; RTN4, reticulon 4; TEM, transmission electron microscopy; UPR, unfolded protein response; XBP1, X-box binding protein-1.

References

1. Porter, K. R., Claude, A., and Fullam, E. F. (1945) A study of tissue culture cells by electron microscopy : Methods and preliminary observations. *J. Exp. Med.* **81**, 233–246
2. Puhka, M., Joensuu, M., Vihinen, H., Belevich, I., and Jokitalo, E. (2012) Progressive sheet-to-tubule transformation is a general mechanism for endoplasmic reticulum partitioning in dividing mammalian cells. *Mol. Biol. Cell* **23**, 2424–2432
3. Palade, G. E. (1955) Studies on the endoplasmic reticulum. II. Simple dispositions in cells *in situ*. *J. Biophys. Biochem. Cytol.* **1**, 567–582
4. Shibata, Y., Shemesh, T., Prinz, W. A., Palazzo, A. F., Kozlov, M. M., and Rapoport, T. A. (2010) Mechanisms determining the morphology of the peripheral ER. *Cell* **143**, 774–788
5. Black, V. H., Sanjay, A., van Leyen, K., Moeller, I., Lauring, B., and Kreibich, G. (2002) Cholesterol and steroid synthesizing smooth endoplasmic reticulum of adrenocortical cells contains high levels of translocation apparatus proteins. *Endocr. Res.* **28**, 425–430
6. Raffaello, A., Mammucari, C., Gherardi, G., and Rizzuto, R. (2016) Calcium at the center of cell signaling: Interplay between endoplasmic reticulum, mitochondria, and lysosomes. *Trends Biochem. Sci.* **41**, 1035–1049
7. Lee, J. E., Cathey, P. I., Wu, H., Parker, R., and Voeltz, G. K. (2020) Endoplasmic reticulum contact sites regulate the dynamics of membraneless organelles. *Science* **367**, eaay7108
8. Wu, H., Carvalho, P., and Voeltz, G. K. (2018) Here, there, and everywhere: The importance of ER membrane contact sites. *Science* **361**, eaan5835
9. Orso, G., Pendin, D., Liu, S., Tosetto, J., Moss, T. J., Faust, J. E., Micaroni, M., Egorova, A., Martinuzzi, A., McNew, J. A., and Daga, A. (2009) Homotypic fusion of ER membranes requires the dynamin-like GTPase atlastin. *Nature* **460**, 978–983
10. Wang, N., and Rapoport, T. A. (2019) Reconstituting the reticular ER network - mechanistic implications and open questions. *J. Cell Sci.* **132**, jcs227611
11. Powers, R. E., Wang, S., Liu, T. Y., and Rapoport, T. A. (2017) Reconstitution of the tubular endoplasmic reticulum network with purified components. *Nature* **543**, 257–260
12. Hu, J., Prinz, W. A., and Rapoport, T. A. (2011) Weaving the web of ER tubules. *Cell* **147**, 1226–1231
13. Voeltz, G. K., Prinz, W. A., Shibata, Y., Rist, J. M., and Rapoport, T. A. (2006) A class of membrane proteins shaping the tubular endoplasmic reticulum. *Cell* **124**, 573–586
14. Shibata, Y., Voss, C., Rist, J. M., Hu, J., Rapoport, T. A., Prinz, W. A., and Voeltz, G. K. (2008) The reticulon and DP1/Yop1p proteins form immobile oligomers in the tubular endoplasmic reticulum. *J. Biol. Chem.* **283**, 18892–18904
15. Joensuu, M., Belevich, I., Ramo, O., Nevzorov, I., Vihinen, H., Puhka, M., Witkos, T. M., Lowe, M., Vartiainen, M. K., and Jokitalo, E. (2014) ER sheet persistence is coupled to myosin 1c-regulated dynamic actin filament arrays. *Mol. Biol. Cell* **25**, 1111–1126
16. Lakkaraju, A. K., Abrami, L., Lemmin, T., Blaskovic, S., Kunz, B., Kihara, A., Dal Peraro, M., and van der Goot, F. G. (2012) Palmitoylated calnexin is a key component of the ribosome-translocon complex. *EMBO J.* **31**, 1823–1835
17. Terasaki, M., Chen, L. B., and Fujiwara, K. (1986) Microtubules and the endoplasmic reticulum are highly interdependent structures. *J. Cell Biol.* **103**, 1557–1568
18. Friedman, J. R., Webster, B. M., Mastronarde, D. N., Verhey, K. J., and Voeltz, G. K. (2010) ER sliding dynamics and ER-mitochondrial contacts occur on acetylated microtubules. *J. Cell Biol.* **190**, 363–375
19. Guo, Y., Li, D., Zhang, S., Yang, Y., Liu, J. J., Wang, X., Liu, C., Milkie, D. E., Moore, R. P., Tulu, U. S., Kiehart, D. P., Hu, J., Lippincott-Schwartz, J., Betzig, E., and Li, D. (2018) Visualizing intracellular organelle and cytoskeletal interactions at nanoscale resolution on millisecond timescales. *Cell* **175**, 1430–1442.e17
20. Klopfenstein, D. R., Kappeler, F., and Hauri, H. P. (1998) A novel direct interaction of endoplasmic reticulum with microtubules. *EMBO J.* **17**, 6168–6177
21. Ogawa-Goto, K., Tanaka, K., Ueno, T., Tanaka, K., Kurata, T., Sata, T., and Irie, S. (2007) p180 is involved in the interaction between the endoplasmic reticulum and microtubules through a novel microtubule-binding and bundling domain. *Mol. Biol. Cell* **18**, 3741–3751
22. Puhka, M., Vihinen, H., Joensuu, M., and Jokitalo, E. (2007) Endoplasmic reticulum remains continuous and undergoes sheet-to-tubule transformation during cell division in mammalian cells. *J. Cell Biol.* **179**, 895–909
23. van Anken, E., and Braakman, I. (2005) Endoplasmic reticulum stress and the making of a professional secretory cell. *Crit. Rev. Biochem. Mol. Biol.* **40**, 269–283
24. Shemesh, T., Klemm, R. W., Romano, F. B., Wang, S., Vaughan, J., Zhuang, X., Tukachinsky, H., Kozlov, M. M., and Rapoport, T. A. (2014) A model for the generation and interconversion of ER morphologies. *Proc. Natl. Acad. Sci. U. S. A.* **111**, E5243–E5251
25. Walter, P., and Ron, D. (2011) The unfolded protein response: From stress pathway to homeostatic regulation. *Science* **334**, 1081–1086
26. Hetz, C., Zhang, K., and Kaufman, R. J. (2020) Mechanisms, regulation and functions of the unfolded protein response. *Nat. Rev. Mol. Cell Biol.* **21**, 421–438
27. Schuck, S., Prinz, W. A., Thorn, K. S., Voss, C., and Walter, P. (2009) Membrane expansion alleviates endoplasmic reticulum stress independently of the unfolded protein response. *J. Cell Biol.* **187**, 525–536

28. Rutkowski, D. T., Wu, J., Back, S. H., Callaghan, M. U., Ferris, S. P., Iqbal, J., Clark, R., Miao, H., Hassler, J. R., Fornek, J., Katze, M. G., Hussain, M. M., Song, B., Swathirajan, J., Wang, J., *et al.* (2008) UPR pathways combine to prevent hepatic steatosis caused by ER stress-mediated suppression of transcriptional master regulators. *Dev. Cell* **15**, 829–840
29. Fleig, L., Bergbold, N., Sahasrabudhe, P., Geiger, B., Kaltak, L., and Lemberg, M. K. (2012) Ubiquitin-dependent intramembrane rhomboid protease promotes ERAD of membrane proteins. *Mol. Cell* **47**, 558–569
30. Lastun, V. L., Grieve, A. G., and Freeman, M. (2016) Substrates and physiological functions of secretase rhomboid proteases. *Semin. Cell Dev. Biol.* **60**, 10–18
31. Zhang, M., Miao, F., Huang, R., Liu, W., Zhao, Y., Jiao, T., Lu, Y., Wu, F., Wang, X., Wang, H., Zhao, H., Ju, H., Miao, S., Wang, L., and Song, W. (2018) RHBDD1 promotes colorectal cancer metastasis through the Wnt signaling pathway and its downstream target ZEB1. *J. Exp. Clin. Cancer Res.* **37**, 22
32. Xu, Z., Wang, R., Li, X., Yang, L., Peng, H., Wang, Y., and Wang, P. (2021) RHBDD1 silencing inhibited cell growth and invasion of non-small cell lung cancer by mediating ZEB1/PI3K/AKT signaling pathway. *J. Mol. Histol.* **52**, 503–510
33. Wunderle, L., Knopf, J. D., Kuhnle, N., Morle, A., Hehn, B., Adrain, C., Strisovsky, K., Freeman, M., and Lemberg, M. K. (2016) Rhomboid intramembrane protease RHBDL4 triggers ER-export and non-canonical secretion of membrane-anchored TGFalpha. *Sci. Rep.* **6**, 27342
34. Song, W., Liu, W., Zhao, H., Li, S., Guan, X., Ying, J., Zhang, Y., Miao, F., Zhang, M., Ren, X., Li, X., Wu, F., Zhao, Y., Tian, Y., Wu, W., *et al.* (2015) Rhomboid domain containing 1 promotes colorectal cancer growth through activation of the EGFR signalling pathway. *Nat. Commun.* **6**, 8022
35. Paschkowsky, S., Recinto, S. J., Young, J. C., Bondar, A. N., and Munter, L. M. (2018) Membrane cholesterol as regulator of human rhomboid protease RHBDL4. *J. Biol. Chem.* **293**, 15556–15568
36. Knopf, J. D., Landscheidt, N., Pegg, C. L., Schulz, B. L., Kuhnle, N., Chao, C. W., Huck, S., and Lemberg, M. K. (2020) Intramembrane protease RHBDL4 cleaves oligosaccharyltransferase subunits to target them for ER-associated degradation. *J. Cell Sci.* **133**, jcs243790
37. Lemberg, M. K., and Freeman, M. (2007) Functional and evolutionary implications of enhanced genomic analysis of rhomboid intramembrane proteases. *Genome Res.* **17**, 1634–1646
38. Munro, S., and Pelham, H. R. (1987) A C-terminal signal prevents secretion of luminal ER proteins. *Cell* **48**, 899–907
39. Carpenter, A. E., Jones, T. R., Lamprecht, M. R., Clarke, C., Kang, I. H., Friman, O., Guertin, D. A., Chang, J. H., Lindquist, R. A., Moffat, J., Golland, P., and Sabatini, D. M. (2006) CellProfiler: Image analysis software for identifying and quantifying cell phenotypes. *Genome Biol.* **7**, R100
40. Hammond, C., Braakman, I., and Helenius, A. (1994) Role of N-linked oligosaccharide recognition, glucose trimming, and calnexin in glycoprotein folding and quality control. *Proc. Natl. Acad. Sci. U. S. A.* **91**, 913–917
41. Olden, K., Pratt, R. M., Jaworski, C., and Yamada, K. M. (1979) Evidence for role of glycoprotein carbohydrates in membrane transport: Specific inhibition by tunicamycin. *Proc. Natl. Acad. Sci. U. S. A.* **76**, 791–795
42. Ron, D., and Walter, P. (2007) Signal integration in the endoplasmic reticulum unfolded protein response. *Nat. Rev. Mol. Cell Biol.* **8**, 519–529
43. Kozutsumi, Y., Segal, M., Normington, K., Gething, M. J., and Sambrook, J. (1988) The presence of malfolded proteins in the endoplasmic reticulum signals the induction of glucose-regulated proteins. *Nature* **332**, 462–464
44. Marciniak, S. J., Yun, C. Y., Oyadomari, S., Novoa, I., Zhang, Y., Jungreis, R., Nagata, K., Harding, H. P., and Ron, D. (2004) CHOP induces death by promoting protein synthesis and oxidation in the stressed endoplasmic reticulum. *Genes Dev.* **18**, 3066–3077
45. Yang, D. S., Tandon, A., Chen, F., Yu, G., Yu, H., Arawaka, S., Hasegawa, H., Duthie, M., Schmidt, S. D., Ramabhadran, T. V., Nixon, R. A., Mathews, P. M., Gandy, S. E., Mount, H. T., St George-Hyslop, P., *et al.* (2002) Mature glycosylation and trafficking of nicastrin modulate its binding to presenilins. *J. Biol. Chem.* **277**, 28135–28142
46. Walter, P., and Blobel, G. (1983) Preparation of microsomal membranes for cotranslational protein translocation. *Methods Enzymol.* **96**, 84–93
47. Song, Y., Hao, Y., Sun, A., Li, T., Li, W., Guo, L., Yan, Y., Geng, C., Chen, N., Zhong, F., Wei, H., Jiang, Y., and He, F. (2006) Sample preparation project for the subcellular proteome of mouse liver. *Proteomics* **6**, 5269–5277
48. Molinari, M., and Helenius, A. (2000) Chaperone selection during glycoprotein translocation into the endoplasmic reticulum. *Science* **288**, 331–333
49. Ikeda, K. N., and Freeman, M. (2019) Spatial proteomics reveal that the protein phosphatase PTP1B interacts with and may modify tyrosine phosphorylation of the rhomboid protease RHBDL4. *J. Biol. Chem.* **294**, 11486–11497
50. Liu, H., Huryn, K. L., Ma, J., and Armstrong, L. (2011) Fast and Gentle Enrichment Assays for Isolating and Staining Native Protein-Cytoskeleton Associations**, Vol. 3**. *Cellutions - The newsletter for Cell Biology Researchers*. Merck Millipore: 11
51. Baas, P. W., Rao, A. N., Matamoros, A. J., and Leo, L. (2016) Stability properties of neuronal microtubules. *Cytoskeleton (Hoboken)* **73**, 442–460
52. Lu, L., Ladinsky, M. S., and Kirchhausen, T. (2009) Cisternal organization of the endoplasmic reticulum during mitosis. *Mol. Biol. Cell* **20**, 3471–3480
53. Friedman, J. R., Dibenedetto, J. R., West, M., Rowland, A. A., and Voeltz, G. K. (2013) Endoplasmic reticulum-endosome contact increases as endosomes traffic and mature. *Mol. Biol. Cell* **24**, 1030–1040
54. Zinszner, H., Kuroda, M., Wang, X., Batchvarova, N., Lightfoot, R. T., Remotti, H., Stevens, J. L., and Ron, D. (1998) CHOP is implicated in programmed cell death in response to impaired function of the endoplasmic reticulum. *Genes Dev.* **12**, 982–995
55. Yamamoto, K., Takahara, K., Oyadomari, S., Okada, T., Sato, T., Harada, A., and Mori, K. (2010) Induction of liver steatosis and lipid droplet formation in ATF6alpha-knockout mice burdened with pharmacological endoplasmic reticulum stress. *Mol. Biol. Cell* **21**, 2975–2986
56. Wu, J., Rutkowski, D. T., Dubois, M., Swathirajan, J., Saunders, T., Wang, J., Song, B., Yau, G. D., and Kaufman, R. J. (2007) ATF6alpha optimizes long-term endoplasmic reticulum function to protect cells from chronic stress. *Dev. Cell* **13**, 351–364
57. Shaffer, A. L., Shapiro-Shelef, M., Iwakoshi, N. N., Lee, A. H., Qian, S. B., Zhao, H., Yu, X., Yang, L., Tan, B. K., Rosenwald, A., Hurt, E. M., Petroulakis, E., Sonenberg, N., Yewdell, J. W., Calame, K., *et al.* (2004) XBP1, downstream of Blimp-1, expands the secretory apparatus and other organelles, and increases protein synthesis in plasma cell differentiation. *Immunity* **21**, 81–93
58. Klopfenstein, D. R., Klumperman, J., Lustig, A., Kammerer, R. A., Oorschot, V., and Hauri, H. P. (2001) Subdomain-specific localization of CLIMP-63 (p63) in the endoplasmic reticulum is mediated by its luminal alpha-helical segment. *J. Cell Biol.* **153**, 1287–1300
59. Senda, T., and Yoshinaga-Hirabayashi, T. (1998) Intermembrane bridges within membrane organelles revealed by quick-freeze deep-etch electron microscopy. *Anat. Rec.* **251**, 339–345
60. Lemberg, M. K., and Adrain, C. (2016) Inactive rhomboid proteins: New mechanisms with implications in health and disease. *Semin. Cell Dev. Biol.* **60**, 29–37
61. Kung, J. E., and Jura, N. (2016) Structural basis for the non-catalytic functions of protein kinases. *Structure* **24**, 7–24
62. Shay, G., Lynch, C. C., and Fingleton, B. (2015) Moving targets: Emerging roles for MMPs in cancer progression and metastasis. *Matrix Biol.* **44-46**, 200–206
63. Otto, G. P., Sharma, D., and Williams, R. S. (2016) Non-catalytic roles of presenilin throughout evolution. *J. Alzheimers Dis.* **52**, 1177–1187
64. De Strooper, B., Iwatsubo, T., and Wolfe, M. S. (2012) Presenilins and gamma-secretase: Structure, function, and role in Alzheimer disease. *Cold Spring Harb. Perspect. Med.* **2**, a006304
65. Olzmann, J. A., and Carvalho, P. (2019) Dynamics and functions of lipid droplets. *Nat. Rev. Mol. Cell Biol.* **20**, 137–155

66. Tadepalle, N., Robers, L., Veronese, M., Zentis, P., Babatz, F., Brodesser, S., Gruszczyk, A. V., Schauss, A., Honing, S., and Rugarli, E. I. (2020) Microtubule-dependent and independent roles of spastin in lipid droplet dispersion and biogenesis. *Life Sci. Alliance* **3**, e202000715
67. Chang, C. L., Weigel, A. V., Ioannou, M. S., Pasolli, H. A., Xu, C. S., Peale, D. R., Shtengel, G., Freeman, M., Hess, H. F., Blackstone, C., and Lippincott-Schwartz, J. (2019) Spastin tethers lipid droplets to peroxisomes and directs fatty acid trafficking through ESCRT-III. *J. Cell Biol.* **218**, 2583–2599
68. Klemm, R. W., Norton, J. P., Cole, R. A., Li, C. S., Park, S. H., Crane, M. M., Li, L., Jin, D., Boye-Doe, A., Liu, T. Y., Shibata, Y., Lu, H., Rapoport, T. A., Farese, R. V., Jr., Blackstone, C., *et al*. (2013) A conserved role for atlastin GTPases in regulating lipid droplet size. *Cell Rep.* **3**, 1465–1475
69. Christova, Y., Adrain, C., Bambrough, P., Ibrahim, A., and Freeman, M. (2013) Mammalian iRhoms have distinct physiological functions including an essential role in TACE regulation. *EMBO Rep.* **14**, 884–890
70. Heigwer, F., Kerr, G., and Boutros, M. (2014) E-CRISP: Fast CRISPR target site identification. *Nat. Methods* **11**, 122–123
71. Ran, F. A., Hsu, P. D., Wright, J., Agarwala, V., Scott, D. A., and Zhang, F. (2013) Genome engineering using the CRISPR-Cas9 system. *Nat. Protoc.* **8**, 2281–2308
72. Schindelin, J., Arganda-Carreras, I., Frise, E., Kaynig, V., Longair, M., Pietzsch, T., Preibisch, S., Rueden, C., Saalfeld, S., Schmid, B., and Tinevez, J. Y. (2012) Fiji: an open-source platform for biological-image analysis. *Nature Methods* **9**, 676–682
73. Liu, P., Jenkins, N. A., and Copeland, N. G. (2003) A highly efficient recombineering-based method for generating conditional knockout mutations. *Genome Res.* **13**, 476–484